







FULL PAPER

Open Access



Microtremor array surveys and development of the velocity model in the Hakodate Plain, Hokkaido, Japan

Kimiyuki Asano^{1*} , Tomotaka Iwata¹ , Kunikazu Yoshida² , Naoto Inoue² , Kazuhiro Somei² , Ken Miyakoshi²  and Michihiro Otori³

Abstract

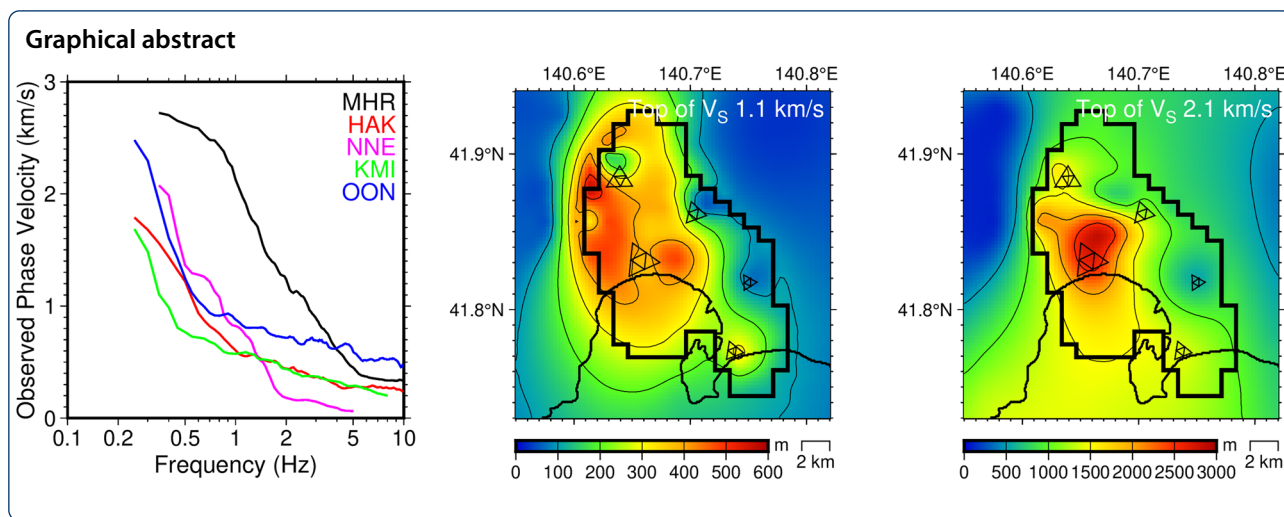
The Hakodate Plain in the southern part of the Oshima Peninsula, Hokkaido, Japan, is a sedimentary basin surrounded by mountains. The vertical displacements caused by active faults along the western margin of the Hakodate Plain increased the basin depth in the western part of the Hakodate Plain. Small-to-large-sized microtremor array surveys were conducted at five sites in the Hakodate Plain to estimate the S-wave velocity structure down to the seismic bedrock for each site to develop a detailed velocity structure model. A new three-dimensional velocity structure model of the Hakodate Plain was developed by integrating the results of microtremor array surveys and other existing geophysical explorations data. This three-dimensional velocity model was modeled as a stack of homogeneous isotropic layers to facilitate its incorporation into the present nation-wide three-dimensional velocity model for ground motion prediction. The bottom depth of the Quaternary sediments is deep along the western margin of the Hakodate Plain. The total thickness of the Quaternary and Neogene sedimentary layers reaches 2.9 km in the western Hakodate Plain. The proposed velocity model was validated by gravity anomaly modeling and ground motion simulation of a moderate-sized inland earthquake. The location of the low-gravity anomaly around the coastline of the Hakodate Bay was improved using the new model. The numerical ground motion simulation using FDM also demonstrated that the amplification and long duration observed in the western part of the Hakodate Plain were reproduced effectively using this velocity model. The spatial variation in long-period ground motion amplifications (period > 1 s) is discussed based on numerical simulations utilizing our three-dimensional velocity model. The highest amplifications at periods of 4 and 5 s were expected in the southwestern Hakodate Plain. The amplification at a period of 3 s was relatively high near the western margin of the plain. Conversely, the spatial characteristics below 2 s were quite complex due to interference of the seismic wavefield inside the basin structure. Variation due to the source location was also relatively high in the shorter period range.

Keywords: Hakodate Plain, Microtremor array survey, Velocity structure model, Ground motion simulation

*Correspondence: k-asano@sms.dpri.kyoto-u.ac.jp

¹ Disaster Prevention Research Institute, Kyoto University, Gokasho, Uji, Kyoto 611-0011, Japan

Full list of author information is available at the end of the article



Main text

Introduction

The Hakodate Plain in the southern part of the Oshima Peninsula, Hokkaido, northern Japan, faces the Tsugaru Strait on the southern side. The area, approximately 12 km in the east–west direction and 15 km in the north–south direction (Fig. 1), is a sedimentary basin surrounded by the Kamiiso Mountains and the Kameda Mountains towards the west and east, respectively. A geological map in and around the Hakodate Plain is shown in Fig. 1b. Active faults named as Oshima-Ono and Tomikawa faults run nearly north to south along the western margin of the plain (Ota et al. 1994). The bedrock of the Hakodate Plain is the Mesozoic Kamiiso Group of the Oshima Belt (e.g., Hata et al. 1984). According to the hot spring boring data drilled at the Ono Town Health Center (H480-020 in Fig. 1a; now called Hokuto Municipal Health Center), the top depth of limestones belonging to the Kamiiso Group is 1325 m (Geological Survey of Hokkaido 2004). The Kamiiso Group is overlain by the Neogene Hekirijigawa Formation with an unconformity. The Neogene Todagawa and Mohejigawa formations, Togheshita pyroclastic rocks, and Pleistocene Tomikawa and Fumizuki formations are deposited above the Hekirijigawa Formation in the sedimentary basin beneath the Hakodate Plain. Alluvium and moor deposits

(peat) are extensively distributed near the surface in the Hakodate Plain (Fig. 1b). Fluvial and marine terraces are distributed along the western and eastern edges of the Hakodate Plain (Ota et al. 1994).

The most remarkable earthquake disaster in the Hakodate Plain in recent decades was caused by the 1968 Tokachi-oki earthquake (M_{JMA} 7.9), a plate-boundary thrust earthquake along the Japan Trench (e.g., Kanamori 1971; Kikuchi and Fukao 1985; Mori and Shimazaki 1985). Its source area was located more than 100 km away from the Hakodate Plain (Fig. 1). During this earthquake, the seismic intensity was 5 in Hakodate on the scale of the Japan Meteorological Agency (JMA). Damage to piers, harbor facilities, and residential houses around the Port of Hakodate, collapse of reinforced concrete buildings, and liquefaction, along with damage to stone walls at Fort Goryokaku have been reported (Hayashi and Katayama 1970; Yoshimi and Akagi 1968; Special Committee for the Investigation of the Tokachi-oki Earthquake 1968 1969).

Besides plate-boundary earthquakes, the Earthquake Research Committee (ERC) of the Headquarters for Earthquake Research Promotion (HERP) published a long-term evaluation of major active faults in Japan. ERC/HERP evaluated that the probability of earthquake occurrence within 30 years in the active fault zone on the western margin of the Hakodate Plain is nearly 0 to 1%, marking A*-rank

(See figure on next page.)

Fig. 1 Index map of the study area. **a** Topographical map drawn using the Digital Map (Basic Geospatial Information) of the Geospatial Information Authority of Japan. **b** Geological map drawn referring to Geological Survey of Japan (2020), Hata et al. (1984), and Shibata et al. (2009). The configurations of large triangle arrays (L array) at each site are shown in the two maps with thin solid lines. The red lines correspond to the active fault traces on the western margin of Hakodate Plain identified in National Institute of Advanced Industrial Science and Technology (AIST) (2019). OF Oshima-Ono Fault, TF Tomikawa Fault. The purple lines represent the reflection survey lines (OSM18-1D and OSM18-2H) by Sato et al. (2019), and solid circles indicate the locations of hot spring wells (H480-017 and H480-020, Geological Survey of Hokkaido 1995). The location of the study area is displayed in the inset map of **a**. The focal mechanism of the 1968 Tokachi-oki earthquake determined by Kanamori (1971) is plotted in the inset map

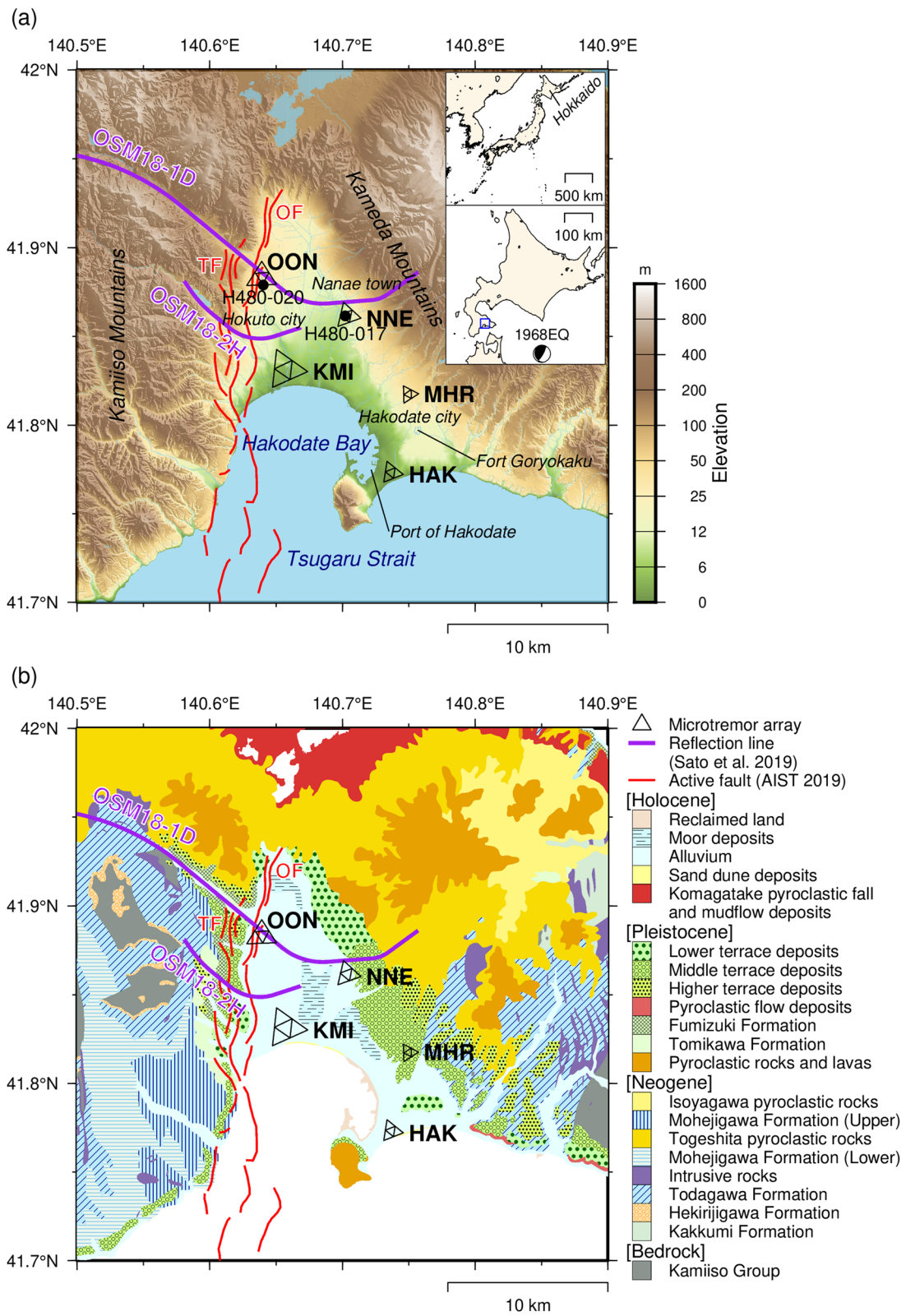


Fig. 1 (See legend on previous page.)

(fairly high probability) as of January 1, 2021 (Earthquake Research Committee 2021a). ERC/HERP also estimated the expected magnitude at M_W 6.6 and published a scenario-based seismic hazard map for this active fault zone. Very severe to destructive ground motions (seismic intensity 6+ to 7 on the JMA scale) are expected in the wide area of the Hakodate Plain (Earthquake Research Committee 2021b; National Research Institute for Earth Science and Disaster Resilience (NIED) 2019c). Thus, the development of a reliable and detailed velocity structure model is important for advancing strong motion prediction and seismic risk assessment in this area. Geophysical explorations data are essential for updating the velocity structure model of the sedimentary plain.

In the Hakodate Plain, geophysical explorations have been conducted for oil and natural gas surveys (Japan National Oil Corporation 1981), active fault research (e.g., Tajika et al. 1999), and geothermal resource research (e.g., Shibata et al. 2009). These past geophysical explorations provided information regarding the geological structure and the P-wave velocity profiles in the Hakodate Plain.

However, the S-wave velocity structure of the deep sedimentary basin, which primarily affects the amplification of ground motions, has not been investigated effectively in this area, except for a pioneering study utilizing single-station microtremor observations by Nogoshi and Igarashi (1971). Therefore, the S-wave velocity structure should be surveyed in the Hakodate Plain to achieve the improvement of the velocity model for quantitative ground motion predictions and hazard assessments.

In this study, we conducted small- to large-scale microtremor array surveys at five sites in the Hakodate Plain and estimated the S-wave velocity structure down to the seismic bedrock for each site. A new three-dimensional velocity structure model of the Hakodate Plain was developed by integrating the results of microtremor array surveys with other existing seismic reflection explorations. Furthermore, the proposed velocity model was validated by gravity anomaly modeling and ground motion simulation of a moderate-sized inland earthquake. Finally, the spatial variation in long-period ground motion amplifications (period > 1 s) is discussed based on numerical simulations utilizing our new three-dimensional velocity model.

Microtremor array survey in the Hakodate Plain

Microtremor array measurements

Microtremor array survey techniques have been widely implemented to explore S-wave velocity structures in sedimentary basins and plains in Japan and other countries (e.g., Asano et al. 2015; Chimoto et al. 2016; Kudo et al. 2002; Mascandola et al. 2019; Yamada et al. 2020). Several previous studies have surveyed S-wave velocity structure of large sedimentary basins in Hokkaido, such

as the Ishikari, Yufutsu, and Kushiro basins (e.g., Arai and Tokimatsu 2008; Okada et al. 1990; Takai et al. 2019). Although Hakodate is the third largest city in Hokkaido, to the best of our knowledge, no microtremor array survey has been conducted in the Hakodate Plain before this study.

In this study, large-scale microtremor array surveys were conducted at five sites in the Hakodate Plain (Fig. 1; Table 1). Four sites were located in the vicinity of permanent strong motion stations of NIED K-NET (HAK), JMA (MHR), or Hokkaido Government (KMI and OON) (Additional file 1: Figs. S1–S4). NNE is a site of hot spring well (H480-017 in Fig. 1 and Additional file 1: Fig. S5), where the geological profile was reported by the Geological Survey of Hokkaido (1995, 2004). According to the geological map in this area (Hata et al. 1984), MHR is located on the middle terrace deposits while the other four sites are on alluvium and moor deposits.

Each array survey consisted of five or six equilateral triangular arrays with different circumscribed circle radii (L, S, and N arrays in Table 1). The minimum array radius (R_{\min}) was 10 or 12 m (N array), and the maximum array radius (R_{\max}) was in the range of 620–1,380 m depending on the expected bedrock depth (L array). Miyakoshi et al. (1996) demonstrated that the maximum wavelength (l_{\max}) at which the phase velocity could be estimated using the SPAC method is approximately 10 times larger than the array radius. Therefore, l_{\max} ranges from about 6.2 km (MHR) to 13.8 km (KMI) in our cases. These array configurations enable us to obtain a phase velocity of more than 2.0 km/s within the measurable frequency range of these array observations, which reflects the S-wave velocity structure of deep sediments down to the basin bedrock (approximately 1–3 km). The array configurations for each site are presented on the maps in Additional file 1: Figs. S1–S5. Each of L and S arrays forms a nested triangular array or a common-base nested triangular array with seven sensors, while each array observation of N arrays consists of a single triangular array with four sensors. A three-component seismograph was installed at each vertex of the equilateral triangle and at the center of the circumscribed circle. Seven servo-type velocity seismometers LE-3D/5 s manufactured by Lennartz-Electronic (800 V/(m/s) in 0.2–50 Hz) were utilized for the L and S arrays, and four portable accelerometers SMAR-6A3P manufactured by AKASHI Corporation (1.1 V/G in 0.07–100 Hz) were utilized for a single triangular array of the N array. Thus, the data from different types of sensors have not been mixed during the data analysis. The analog amplifier in SMAR-6A3P was set to $\times 1,000$. The microtremor was continuously recorded by a 24-bit A/D data logger (DATAMARK LS-8800, Hakusan Corporation) and synchronized by the global positioning system

Table 1 Summary of the microtremor array observations in the Hakodate Plain

Site	Size	Radius (m)	Center of circumscribed circle		Observation date and time
			Latitude (°N)	Longitude (°E)	
HAK	N	10	41.77032	140.73830	2017/9/25 13:20–13:46
	S	40, 120	41.77048	140.73829	2017/9/25 15:35–16:35
	L	380, 760	41.77326	140.73688	2017/9/25 11:25–13:15
MHR	N	10	41.81762	140.75182	2017/9/28 10:50–11:15
	S	28, 92	41.81795	140.75214	2017/9/28 10:15–11:00
	L	310, 620	41.81741	140.74990	2017/9/28 11:50–13:30
KMI	N	12, 29	41.82532	140.65311	2017/9/27 11:20–12:53 2017/9/27 13:20–13:55
	S	83, 249	41.82541	140.65253	2017/9/27 10:50–11:30
	L	690, 1380	41.83135	140.65713	2017/9/27 12:10–13:30
OON	N	10, 30	41.88390	140.64473	2017/9/26 11:00–12:00 2017/9/26 12:27–13:20
	S	90, 180	41.88426	140.64453	2017/9/28 14:40–15:20
	L	490, 980	41.88344	140.63994	2017/9/28 16:05–17:05
NNE	N	10	41.86187	140.70154	2017/9/27 18:30–19:00
	S	58, 174	41.86209	140.70156	2017/9/27 18:10–19:00
	L	444, 888	41.86150	140.70360	2017/9/27 15:20–17:00

clock. The sampling frequency was 100 Hz; thus, the cut-off frequency of the decimation filter within LS-8800 was 40 Hz. A huddle test was conducted before starting observation in the field (Additional file 1: Fig. S6), and we confirmed that the signal coherence among sensors was sufficient in the target frequency range (Additional file 1: Figs. S7 and S8). The fieldwork was conducted on September 25–28, 2017. Table 1 summarizes the microtremor array observations.

The vertical component of the recorded microtremors was analyzed to obtain the spatial autocorrelation (SPAC) coefficients (Aki 1957) after dividing the records into many small time-segments. The SPAC coefficient $\rho(f, r)$ can be associated with the phase velocity $c(f)$ via the Bessel function of the first kind J_0 (Aki, 1957; Okada 2003):

$$\rho(f, r) = J_0(rk) = J_0\left(\frac{2\pi fr}{c(f)}\right), \tag{1}$$

where f is the frequency, k is the wavenumber, and r is the distance between sensors in an array. The length of each time-segment is 40.96 s for L and S arrays. For the N array the length of each time-segment is 20.48 s. Nine datasets each consisting of five time-segments were selected for each array by visually inspecting segments that were not contaminated by nonstationary noises, such as heavy traffic noises and other causes. The Fourier spectra of each time-segment was smoothed using a Parzen window, and its bandwidth was selected between 0.15 Hz and 0.78 Hz depending on the size of the array. The phase velocity $c(f)$ at each frequency f was estimated for each dataset using the extended SPAC method (Ling and Okada 1993; Okada 2003), which has been used in

microtremor array surveys at many sites in Japan (e.g., Asano et al. 2015; Goto et al. 2009; Miyakoshi et al. 2021; Ohori et al. 2002; Takahashi et al. 2019; Yoshida and Uebayashi 2020) and other countries (e.g., Ali and Kim 2018; Apostolidis et al. 2004; Foti et al. 2011; Rosa-Cintas et al. 2011; Xu et al. 2013). Since we have several array observations with different distances at each site, the SPAC coefficients $\rho(f, r)$ were obtained for variable r for a fixed frequency f_0 . Thus, the optimum Bessel function of the first kind $J_0(rk)$ as a function of r can be determined using the least square method. Then, the phase velocity $c(f_0)$ can be uniquely obtained by the following Eq. (2) (Ling and Okada 1993; Okada 2003):

$$c(f_0) = \frac{2\pi f_0}{k}. \tag{2}$$

The circles in Fig. 2 represent the estimated phase velocity for each dataset in L, S, and N arrays at each site. The average value of the phase velocity for each frequency point were estimated by combining the results from all arrays, and the estimated dispersion curve was plotted with the black solid line in Fig. 2.

The phase velocity was estimated at up to 5 Hz for NNE and 10 Hz for the other sites (solid lines in Fig. 2). The phase velocity of approximately 65 m/s in the high-frequency range around 5 Hz at NNE is exceptionally low among the five measurement sites, which might be affected by the existence of a peat layer (moor deposits) in that area. The MHR located on the middle terrace contains a relatively larger phase velocity in the lower frequency range below 3 Hz (Fig. 2), which might be attributed to the lack of alluvium deposits in this area.

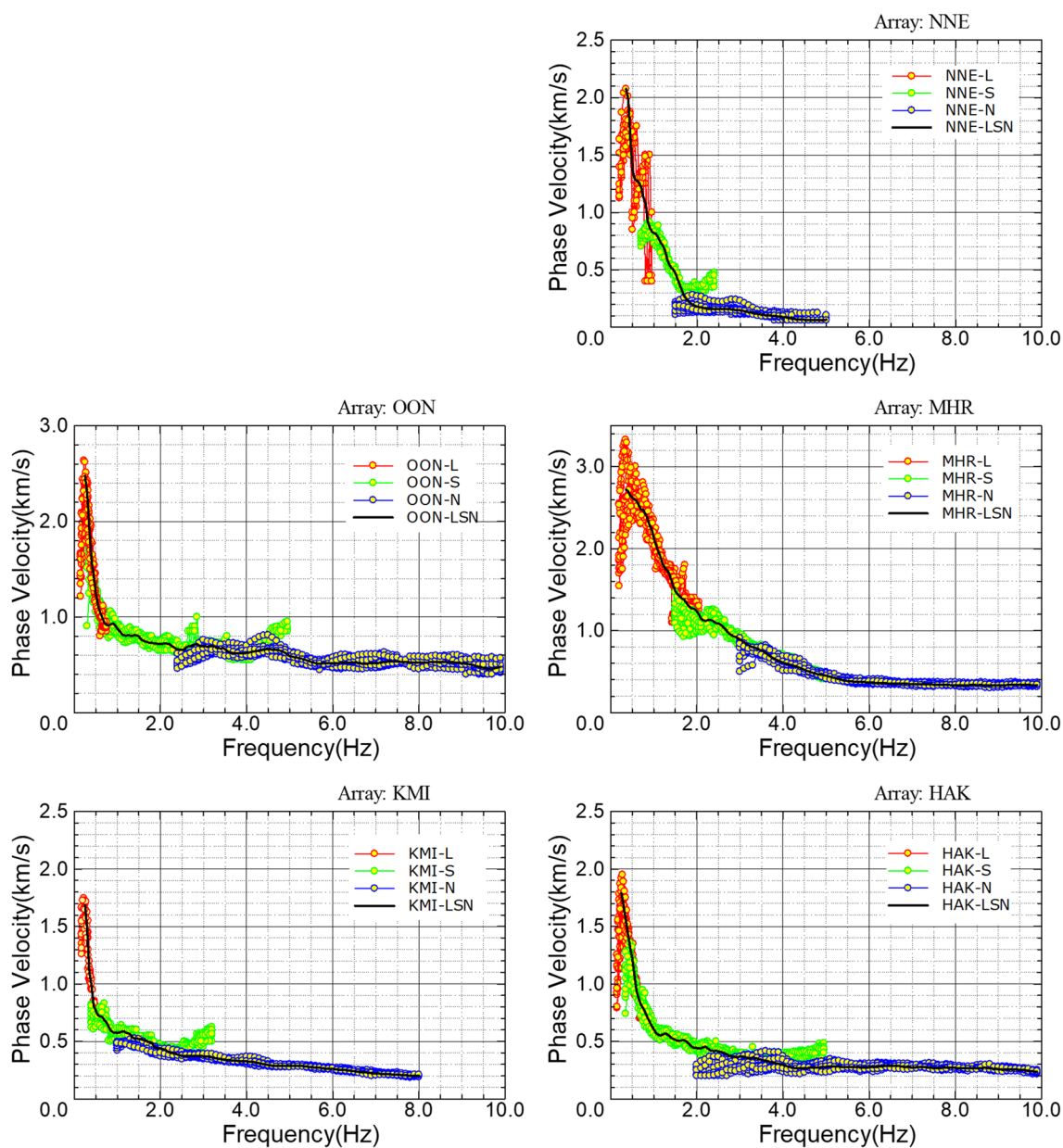


Fig. 2 Observed phase velocities at each site obtained by the SPAC method. The red, green, and blue circles display the measured phase velocities for each dataset from L, S, and N array, respectively. The solid line represents the phase velocity dispersion curve obtained by combining the phase velocities from all datasets of all arrays

Estimation of S-wave velocity structure model

The one-dimensional layered S-wave velocity structure model was estimated at each site by modeling the observed phase velocity as the fundamental mode of the Rayleigh wave. The S-wave velocity of each layer was fixed at the value given in the layered model of J-SHIS V2 (Fujiwara et al. 2012; NIED 2019c) except for few additional layers (Additional file 1: Table S1). The velocity layer of V_s 3.1 km/s was half space. The additional layers were necessary for reproducing

the observed dispersion curves: one or two additional layers corresponding to near-surface low-velocity layers were assigned above the layer of V_s 0.6 km/s (Layers A1 and A2 in Additional file 1: Table S1). Another additional layer was introduced between V_s 0.6 km/s and 1.1 km/s for OON and KMI (Layer A3 in Additional file 1: Table S1). The thickness of each sedimentary layer and the S-wave velocity of the additional layers were estimated using a genetic algorithm (GA) (Yamanaka and Ishida 1996), and their search ranges

are summarized in Additional file 1: Table S1. The density and P-wave velocity during the GA search were given by the empirical relationships with S-wave velocity of Ludwig et al. (1970).

The misfit between the theoretical and observed dispersion curves was evaluated using the following misfit function $f(\mathbf{m})$ during the GA search:

$$f(\mathbf{m}) = \frac{1}{N} \sum_{i=1}^N (O_i - C_i(\mathbf{m}))^2 \left(\frac{\sigma_0}{\sigma_i + w_0} \right)^2, \quad (3)$$

where O_i is the observed phase velocity at frequency point i , and $C_i(\mathbf{m})$ is the theoretical phase velocity

based on a model \mathbf{m} . σ_i is the standard deviation of the observed phase velocity, and w_0 is a parameter implemented to avoid the effects of excessively small σ_i values, and we used $w_0 = 0.01$. σ_0 is a coefficient that is equal to the maximum value of $(\sigma_i + w_0)$. The number of populations in one generation in the GA search was 10. The evolution process terminated at 5,000 generations. This GA run was repeated 10 times by randomly changing the initial member. Furthermore, the solution recording the minimum misfit value $f(\mathbf{m})$ was selected as the best solution, which is plotted with the red line in Fig. 3.

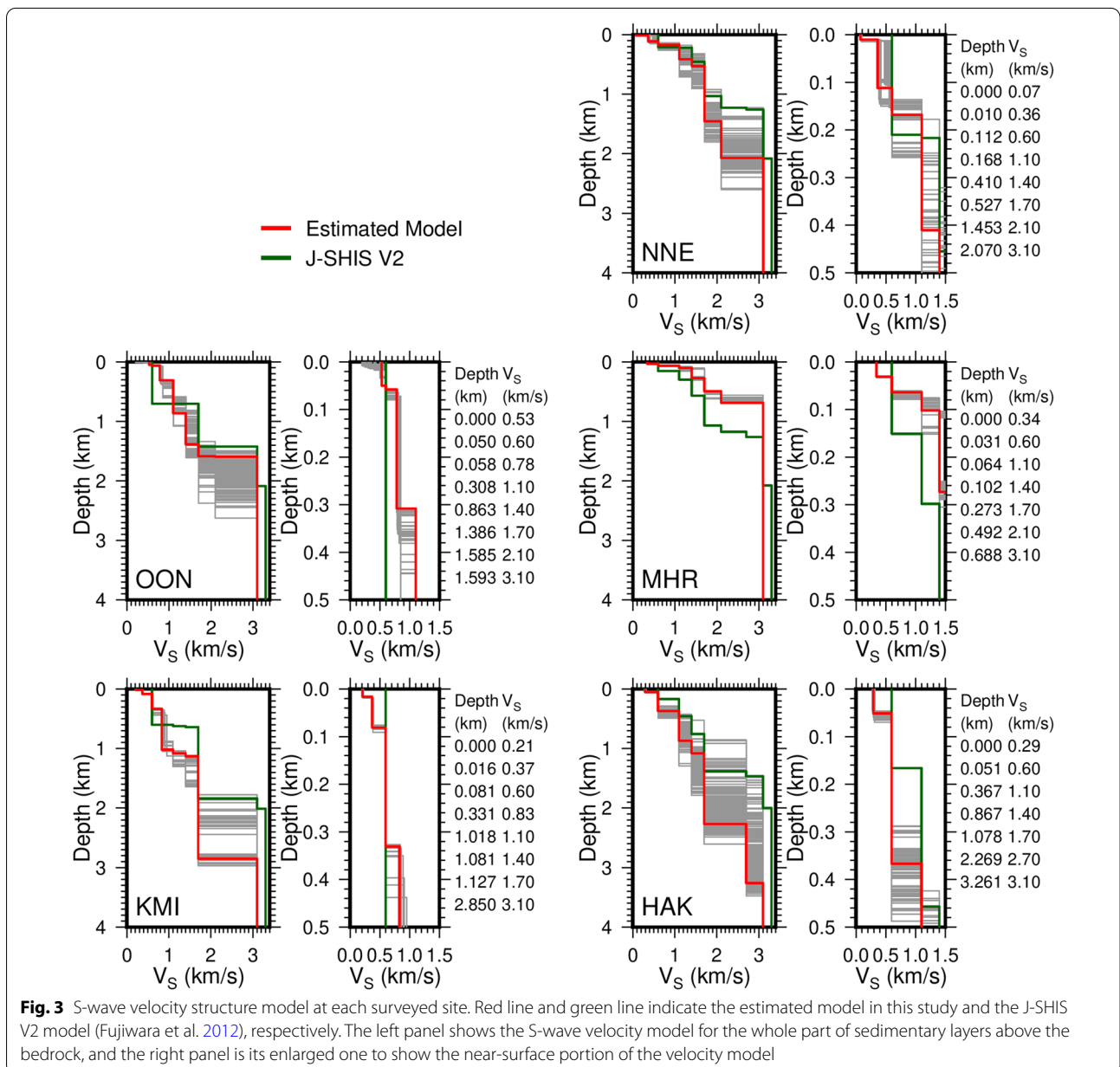


Fig. 3 S-wave velocity structure model at each surveyed site. Red line and green line indicate the estimated model in this study and the J-SHIS V2 model (Fujiwara et al. 2012), respectively. The left panel shows the S-wave velocity model for the whole part of sedimentary layers above the bedrock, and the right panel is its enlarged one to show the near-surface portion of the velocity model

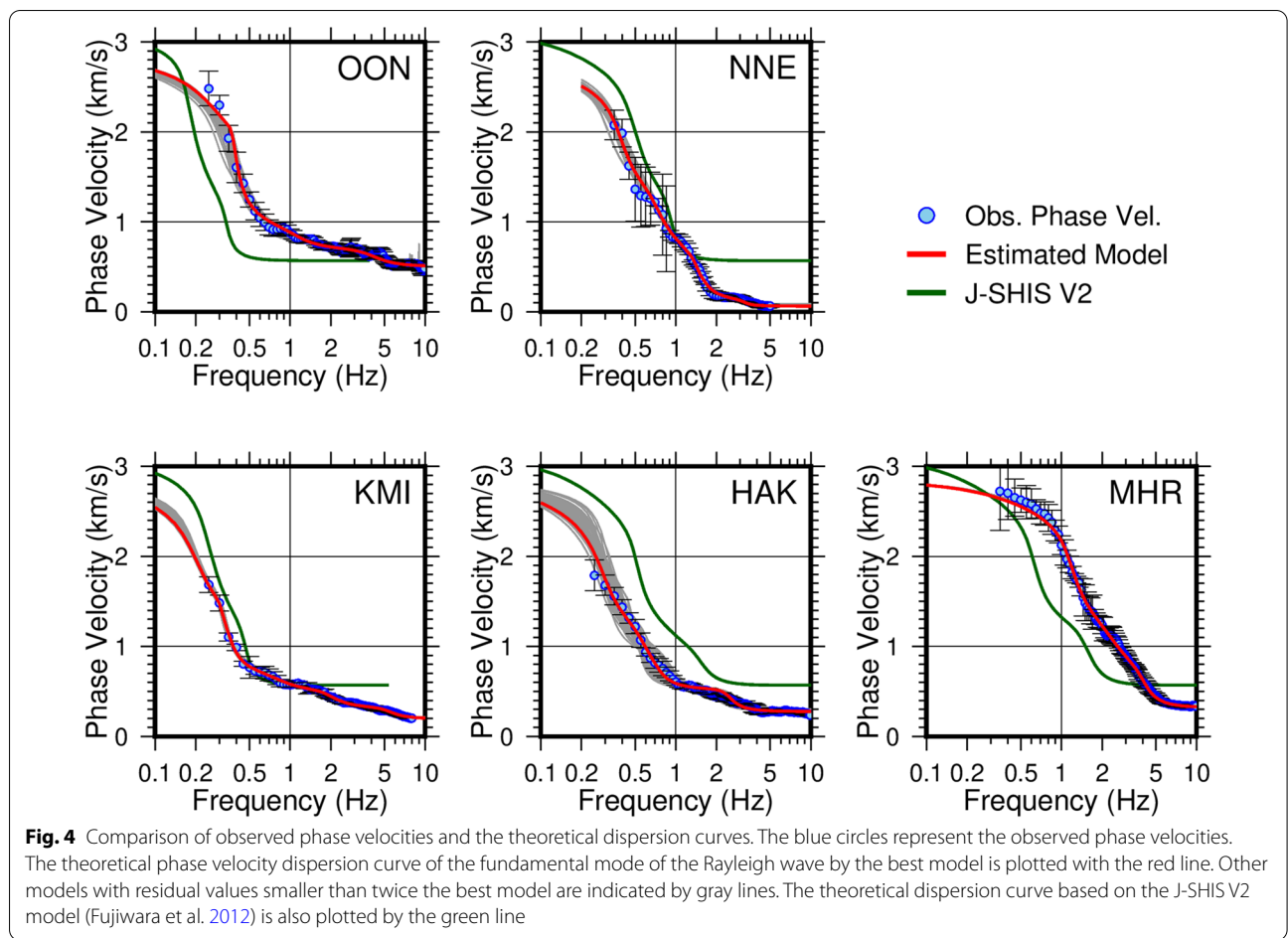
Figure 4 shows the theoretical dispersion curve of the fundamental mode of the Rayleigh wave calculated from the best model (red line) and the observed phase velocities (blue circles). The theoretical dispersion curve of the Rayleigh wave phase velocity was calculated using DISPER80 (Saito, 1988). The other solutions whose misfit values are not more than twice the best solutions are plotted by gray lines in Figs. 3 and 4 to assess the uncertainty of the estimated model. The S-wave velocity model and dispersion curve based on the J-SHIS V2 model are also displayed in these figures for comparison. The theoretical dispersion curve of the velocity model estimated in this study provides better results for the observed model than the J-SHIS V2 model, for all stations.

The observed phase velocity was much higher than the theoretical phase velocity of the J-SHIS V2 model for MHR in Fig. 4; thus, the upper depths of each velocity layer for this site were estimated to be shallower than the J-SHIS V2 model during the GA search. The estimated bedrock depths of the two sites in Hakodate city, HAK (2.3 km) and MHR (0.69 km), were significantly different,

reflecting the difference in the observed phase velocities (Fig. 4).

Two low-velocity layers ($V_s = 0.07$ km/s and 0.36 km/s) were required to explain the observed phase velocity for NNE, and the thicknesses of these low-velocity layers are much larger than those of the other sites. These low-velocity layers correspond to sand, gravel, clay and volcanic ash layers found in the hot spring well (Additional file 1: Fig. S9). The topmost velocity layer ($V_s = 0.07$ km/s) might be related to the distribution of the peat layer in this area.

One additional velocity layer between $V_s = 0.6$ km/s and 1.1 km/s was required for explaining the observed phase velocity at two sites in the western part of the Hakodate Plain (KMI and OON). The S-wave velocity of this additional layer was approximately 0.8 km/s. The estimated thickness of three layers of $V_s = 0.6$, 1.1 , and 1.4 km/s are thicker for OON and KMI compared to NNE in the eastern part of the plain. These results are also supported by difference in thickness of the Tomikawa, Mohejigawa, and Todagawa formations between two hot spring wells (Additional file 1: Fig. S9). The



estimated seismic bedrock depth (1.6 km) at OON is consistent with the refraction survey utilizing P-waves from explosion sources of quarry blasting analyzed by Takanami and Yamauchi (1996).

Construction of the three-dimensional velocity model in the Hakodate Plain

Datasets

The three-dimensional velocity structure model in the Hakodate Plain was constructed by compiling available geophysical exploration data. The target area for our modeling is represented by the geographical area surrounded by the red frame in Fig. 5. This was defined by considering the spatial distribution of available geophysical exploration information (microtremor array and seismic reflection surveys), basin structure in the initial model, geology, and surface topography. The J-SHIS V2 model (Fujiwara et al. 2012; NIED 2019c) was utilized as the initial model for the present study (Figs. 6 and 7). The J-SHIS V2 model is a nation-wide three-dimensional velocity model covering the Japanese territory developed for ground motion prediction in national seismic hazard maps. It consists of several homogeneous isotropic layers above the seismic bedrock ($V_p=6.0$ km/s and $V_s=3.4$ km/s). The newly constructed model was fitted into the J-SHIS V2 model by replacing the existing model inside the Hakodate Plain with the new one. Thus, the material parameters (P- and S-wave velocities and density, listed in Table 2) in each homogeneous isotropic velocity layer in the new model also follow the J-SHIS V2 model.

The S-wave velocity models obtained by the microtremor array surveys in our study were utilized to develop the new model. The additional layer ($V_s \sim 0.8$ km/s) found at two sites (KMI and OON) were merged into the layer of $V_s=0.6$ km/s as its spatial extent remains to be determined. The seismic reflection surveys using explosion sources by the Japan National Oil Corporation (1981) and the seismic reflection and refraction surveys across the Oshima Peninsula by Sato et al. (2019) were also utilized to constrain the depths of the layer boundaries. Sato et al. (2019) utilized four to five vibroseis trucks as the controlled source for the deep seismic line OSM18-1D and a vibroseis truck for the high-resolution seismic reflection line OSM18-2H across the active faults (Fig. 1). Their survey revealed that the depth to the surface of pre-Tertiary rocks deepened to the west, and it was more than 2 km at the deepest part of the basin. Furthermore, the Neogene sediments are observed to be relatively thick in the western Hakodate Plain.

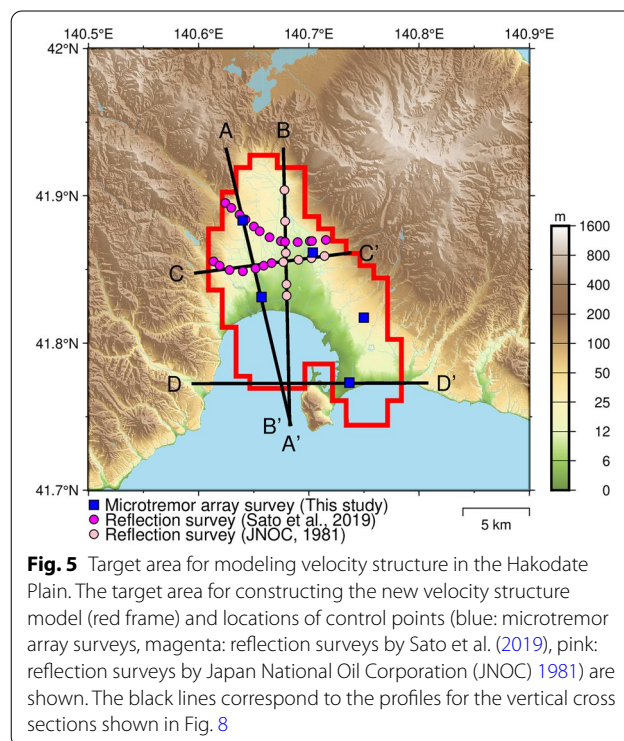
We compared the geologically interpreted seismic profiles of Sato et al. (2019), hot spring well logs (Additional file 1: Fig. S9), and microtremor array survey

results (Fig. 3), and assigned the S-wave velocity to the geological structure. The bottom depth of $V_s=0.6$ km/s layer corresponds to the bottom depth of the Quaternary sediments. The bottom depth of $V_s=1.1$ km/s layer was assumed as the boundary depth between the Neogene Mohejigawa and Todagawa formations. We interpreted that the bottom depths of $V_s=1.4$ km/s and 1.7 km/s layer correspond to the bottom depth of the Todagawa Formation and Neogene sediments, respectively.

The total number of control points, where data were provided to control the interpolation of the layer boundaries, was 34. Five control points were based on the microtremor array surveys. Nine control points were extracted from the seismic reflection results of Japan National Oil Corporation (1981), while 20 control points were extracted from the seismic reflection surveys of Sato et al. (2019). The locations of these control points are indicated on the map in Fig. 5. The bottom depth of each velocity layer at the control points along the four representative profile lines is plotted in the vertical cross sections in Fig. 8. The spatial distribution of the control points in the plain is not uniform due to the limited available information. In particular, there are few available control points in the southeastern part of the Hakodate Plain.

Procedure for velocity structure modeling

The horizontal mesh size of the developed velocity model as well as the J-SHIS V2 model is 30 arc-seconds



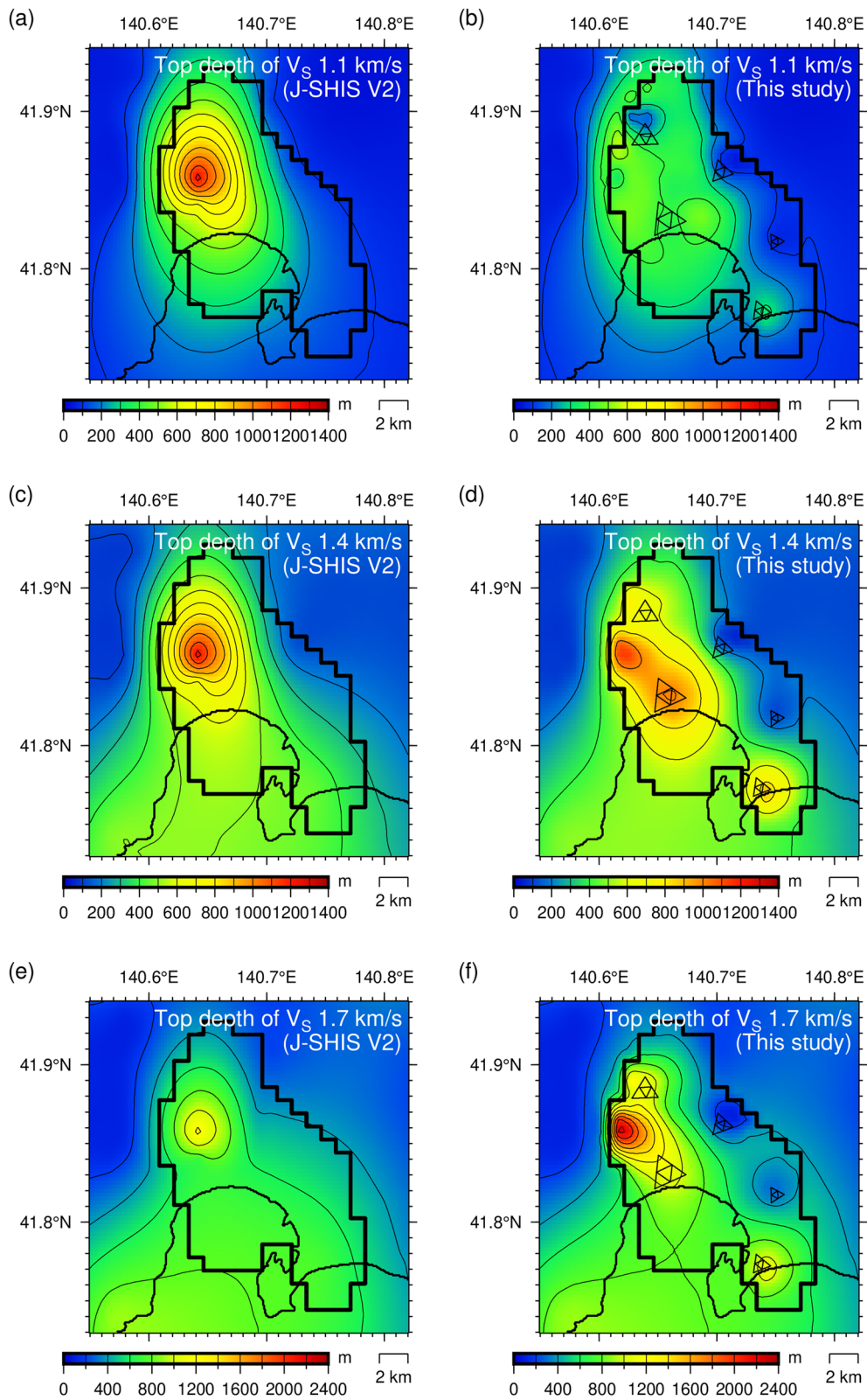


Fig. 6 Depth distributions of the top surface of each velocity layer. **a** $V_S = 1.1$ km/s of J-SHIS V2 model, **b** $V_S = 1.1$ km/s of this study, **c** $V_S = 1.4$ km/s of J-SHIS V2 model, **d** $V_S = 1.4$ km/s of this study, **e** $V_S = 1.7$ km/s of J-SHIS V2 model, **f** $V_S = 1.7$ km/s of this study. The black frame represents the target area of the velocity structure modeling. The triangles indicate the microtremor array survey sites

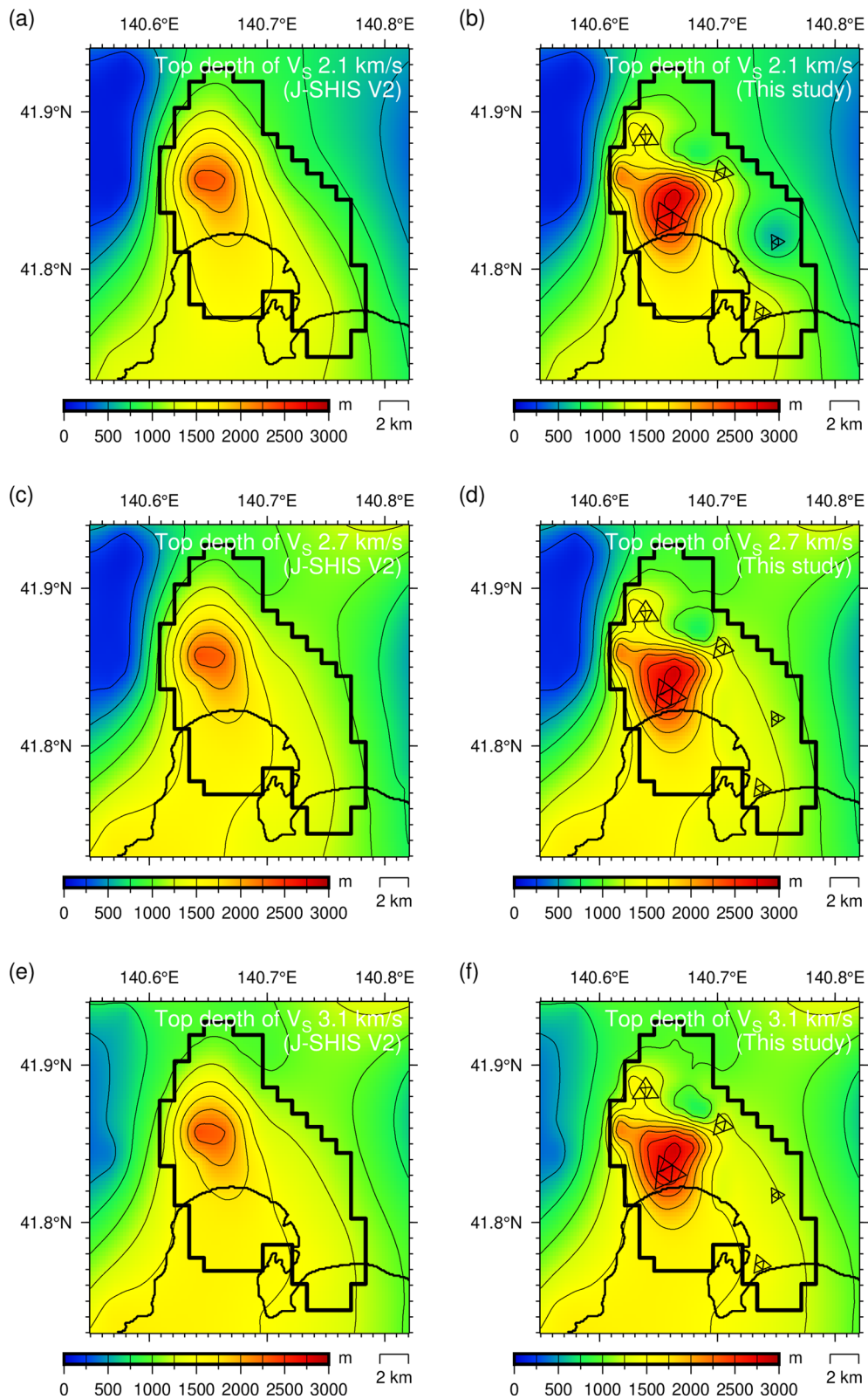


Fig. 7 Depth distributions of the top surface of each velocity layer. **a** $V_S = 2.1$ km/s of J-SHIS V2 model, **b** $V_S = 2.1$ km/s of this study, **c** $V_S = 2.7$ km/s of J-SHIS V2 model, **d** $V_S = 2.7$ km/s of this study, **e** $V_S = 3.1$ km/s of J-SHIS V2 model, **f** $V_S = 3.1$ km/s of this study. The black frame represents the target area of the velocity structure modeling. The triangles indicate the microtremor array survey sites

Table 2 Assumed P- and S-wave velocities and density for each layer

Layer no.	P-wave velocity (km/s)	S-wave velocity (km/s)	Density (g/cm ³)
1	2.0	0.6	1.90
2	2.5	1.1	2.15
3	3.0	1.4	2.25
4	3.5	1.7	2.30
5	4.0	2.1	2.40
6	5.0	2.7	2.50
7	5.5	3.1	2.60
8	5.7	3.3	2.70
9	6.0	3.4	2.75

latitude \times 45 arc-seconds longitude (approximately 1 km \times 1 km). Firstly, the gridded data of the depth information of each velocity layer in and around the target area were prepared from the initial model. Further, we removed all the gridded data within the target area (Fig. 5) and added the control points to the dataset. The surface shape of each homogeneous isotropic velocity layer was modeled using the spline interpolation proposed by Smith and Wessel (1990), implemented in the Generic Mapping Tools software (Wessel et al. 2019). The tension parameter to the gridding equation was set to 0, which provided the minimum curvature solution (Smith and Wessel 1990).

Figures 6 and 7 display the contour maps of the surface depths for each homogeneous isotropic velocity layer ($V_S = 1.1, 1.4, 1.7, 2.1, 2.7,$ and 3.1 km/s), while Fig. 8 demonstrates the vertical cross sections for four representative profiles across the Hakodate Plain, whose locations are indicated on the map in Fig. 5. The deepest area for the top depth of the second layer ($V_S = 1.1$ km/s) or the bottom depth of the first layer ($V_S = 0.6$ km/s) is distributed along the western margin of the Hakodate Plain. Its depth reaches 0.56 km at the deepest location. This spatial distribution could be predominantly interpreted as the result of the Quaternary fault displacements along the active faults on the western margin of the Hakodate Plain. The top depths of $V_S = 1.4$ km/s and 1.7 km/s are also relatively deep in the western part of the Hakodate Plain. The bottom depth of the layer pertaining to $V_S = 1.7$ km/s, which corresponds to the bottom depth of Neogene sediments, deepens towards the coast. Its maximum depth is approximately 2.9 km. The total thickness of the sedimentary layers is relatively small on the eastern margin of the plain, where the lower and middle terraces developed.

Validations and discussion

Validation by simulation of gravity anomaly

The theoretical gravity anomaly was computed based on the newly developed three-dimensional velocity structure model and further compared with the observed Bouguer anomaly. The observed Bouguer anomaly map with an assumed density of 2.3 g/cm³ from the Gravity Database of Japan (Geological Survey of Japan 2013) is plotted in Fig. 9a. The center of the low-gravity anomaly is observed on the coast of Hakodate Bay, southwest of the Hakodate Plain. The Bouguer anomaly in this area is approximately 40 mgal. This low-gravity anomaly area is narrow in the east–west direction and extends northwestward in the Hakodate Plain. The bedrock offset caused by active faults along the western margin of the Hakodate Plain produces a steep gravity change.

The theoretical gravity anomaly was computed using the method of Plouff (1976) considering the surface topography. Figure 9b and c presents the theoretical gravity anomaly for the J-SHIS V2 model and new model of this study, respectively. The density of each layer in our revised model is listed in Table 2, which follows the model parameters of J-SHIS V2 (Fujiwara et al. 2012). The location of the low-gravity anomaly based on the revised model appears better than that of the J-SHIS V2 model. However, the gravity change along the eastern margin of the Hakodate Plain is spatially smoother than the observed gravity anomaly. This is due to limited available information to constrain the bedrock shape along the eastern margin of the plain. The basin shape in the eastern part of the Hakodate Plain needs to be improved by further geophysical exploration, since the precise geometry of the basin edge might affect the generation of basin-induced surface waves during large earthquakes.

Validation by ground motion simulation of a moderate-size earthquake

The three-dimensional velocity structure model was validated by simulating ground motions from a moderate-sized earthquake occurring in Uchiura Bay, Hokkaido (Fig. 10). The target earthquake was a crustal earthquake of M_{JMA} 5.3 on 14:21, June 16, 2016 (JST = UTC + 9). The focal mechanism of this earthquake is thrust-type with a north–south strike angle (Ichiyanagi et al. 2017). A three-dimensional ground motion simulation was conducted utilizing the finite difference method (FDM) of the velocity-stress formulation in the staggered-grid scheme, which was similar to that utilized in Asano et al. (2016). The surface topography was squashed (Aagaard et al. 2008) in this FDM simulation. The computational domain consists of a volume of 48 km along the east–west axis,

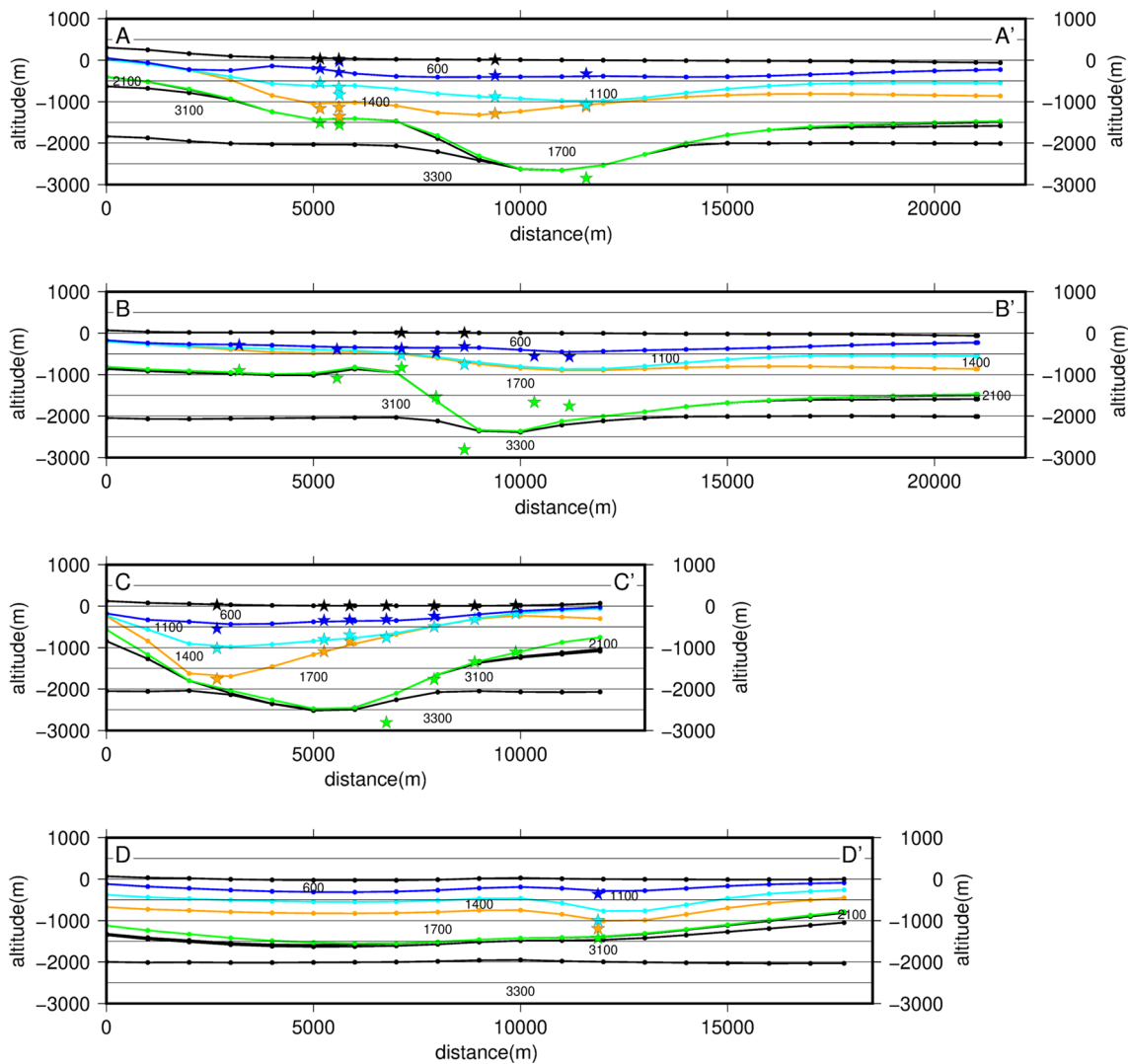
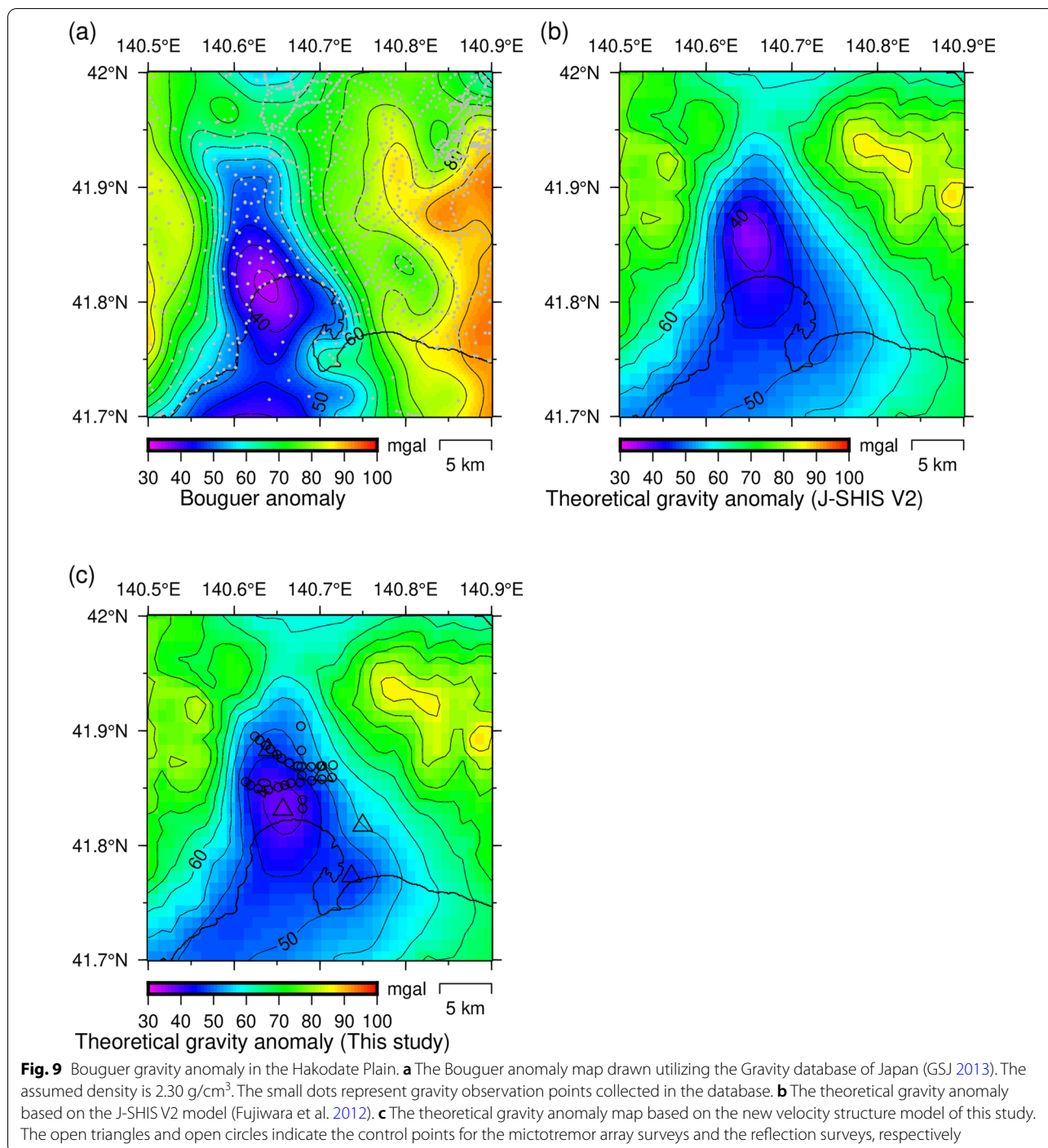


Fig. 8 Vertical cross sections of the velocity structure model developed in this study. The locations of the profiles are displayed on the map in Fig. 5. The black line represents the ground surface, and the black stars indicate the locations of control points on the ground surface. Each color line represents the bottom depth of each velocity layer in our estimated three-dimensional velocity model, and each color star indicates the bottom depth of each velocity layer of input data given at each control point (dark blue: $V_S = 0.6$ km/s, sky blue: $V_S = 1.1$ km/s, orange: $V_S = 1.4$ km/s, green: $V_S = 1.7$ km/s). The number corresponds to the S-wave velocity of each layer. The small dots are placed at every 1 km along the profile line as a kind of tick mark

39 km along the north–south axis, and 29.94 km along the vertical axis (Fig. 10). The volume was discretized using a uniform grid spacing of 30 m. The total number of the grid points is 2,082,901,000 ($1601 \times 1,301 \times 1,000$). The inelastic attenuation was introduced by the technique of Graves (1996), and its reference frequency was set to 1.0 Hz. The minimum S-wave velocity of this velocity model was 0.6 km/s. Thus, the effective maximum frequency of the FDM simulation is approximately 2 Hz in this simulation setting, which results in 10 grids per minimum wavelength.

The epicenter was fixed at the location determined by JMA (JMA 2020), and a moment tensor point-source was introduced according to the routine moment tensor solution by NIED F-net (Aoi et al. 2020; NIED 2019a). The seismic moment was 6.83×10^{16} Nm and the hypocenter depth was 5 km. The source time function was given by the bell-shape function (half period of a sine function), with a duration of 1.7 s based on preliminary analysis. Table 3 summarizes the source parameters utilized in the simulation. The time step in the FDM simulation was



0.002 s to ensure the stability condition, and a wavefield of 60 s was simulated from the origin time.

The observed waveform data at eight strong motion stations (Fig. 10) were collected for comparison with the simulated waveforms, which included two NIED K-NET stations (HKD156 and HKD160), one NIED KiK-net station (OSMH02), two JMA stations (JMA843 and

JMAD66), two seismic intensity stations of the Hokkaido Government (HKDP08 and HKDP09), and one station (BRIHKD) of the Building Research Institute. The station codes for Hokkaido Government stations are not official. HKDP08 represents the seismic intensity station installed at Chuo of Hokuto city, while HKDP09 represents another one installed at Honmachi of Hokuto city.

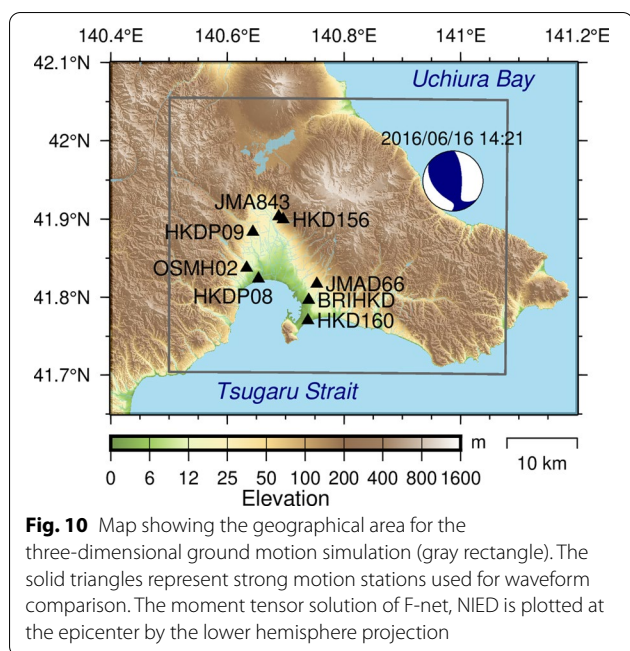


Table 3 Summary of source parameters in the ground motion simulation

Parameter	Value	Reference
Origin time	2016/6/16 14:21:28.20	JMA
Latitude	41.9485°N	JMA
Longitude	140.9870°E	JMA
Moment tensor depth	5 km	NIED F-net
Moment tensor	$M_{rr} = 4.3823 \times 10^{16}$ Nm $M_{tt} = -0.3924 \times 10^{16}$ Nm $M_{\phi\phi} = -4.7747 \times 10^{16}$ Nm $M_{rt} = 1.4970 \times 10^{16}$ Nm $M_{r\phi} = 3.6349 \times 10^{16}$ Nm $M_{t\phi} = 3.1988 \times 10^{16}$ Nm	NIED F-net
Seismic moment	6.83×10^{16} Nm (M_w 5.2)	NIED F-net
Source duration	1.7 s	This study

Figure 11 displays a waveform comparison between the simulated and observed velocity waveforms in the frequency range of 0.1–1 Hz. The simulated waveforms based on the J-SHIS V2 model (Fujiwara et al. 2012) was also plotted for comparison. The relatively long ground motion durations at HKDP08, HKDP09, and OSMH02 in the western part of the Hakodate Plain were well reproduced via this ground motion simulation. The overestimation of amplitude at HKDP09 in the J-SHIS V2 model was improved using our new model. A quantitative evaluation with the Goodness-of-Fit (GOF) criterion proposed by Anderson (2004) were demonstrated for the peak ground velocity (PGV) in five frequency bands for each component of each station in Additional file 1: Fig. S10. The average value of GOF was obtained

by averaging the scores of waveforms filtered in each of the valid frequency band following Anderson (2004). We evaluated five frequency bands (0.05–0.1 Hz, 0.1–0.2 Hz, 0.2–0.5 Hz, 0.5–1 Hz, and 1–2 Hz). The simulated results were quantitatively improved using our new velocity model, and most results fall in excellent or good evaluation. The improvement was not significant for JMA843 and HKD156 located in northmost part of the Hakodate Plain, since available geophysical explorations data are limited.

Comparison of the Fourier amplitude spectra of each component is shown in Fig. 12. The Fourier amplitude spectra were calculated for the whole waveforms of 60 s from the origin time as same as the waveform plot in Fig. 11. The overestimation of amplitude spectra between 0.3 and 0.8 Hz was not improved for JMA843 and HKD156 due to the above-mentioned reason. The systematic underestimation in high frequency above approximately 1 Hz were found for most stations, and we think that this underestimation was mainly caused by the lack of the low-velocity sediments ($V_s < 0.6$ km/s) in our simulation model. The result indicates that modeling of near-surface low-velocity sediments is necessary for improving ground motion simulation particularly above 1 Hz in the Hakodate Plain.

Spatial variation in long-period ground motion amplification

The deep sedimentary basin structure and thickness of soft sediments control the spatial variation in long-period ground motions during mega-thrust earthquakes (Hatayama et al. 2007). The Hakodate Plain may suffer from long-period ground motions from large earthquakes occurring in the Sea of Japan and the Japan Trench. To analyze the spatial variation in long-period ground motion amplification in the Hakodate Plain, we performed 16 pairs of ground motion simulations. The shortest target period for these analyses was 1 s. One simulation pair consisted of one simulation with three-dimensional sedimentary layers in the Hakodate Plain (basin model) and another simulation without sedimentary layers (rock model). The location of the point-source was different for each pair, as displayed in Fig. 13a and Table 4. These 16 cases were a combination of eight epicenters and two different depths. Other source parameters were the same as those in the ground motion simulation presented in the preceding subsection. The source mechanism will not significantly affect the results of this analysis as it will be canceled out in the later part of this analysis. The computational domain was extended to a volume of 100 km along the east–west axis, 96 km along the north–south axis, and 29.9 km along the vertical axis. The volume was discretized using a uniform grid spacing of 50 m. The total number of grid points

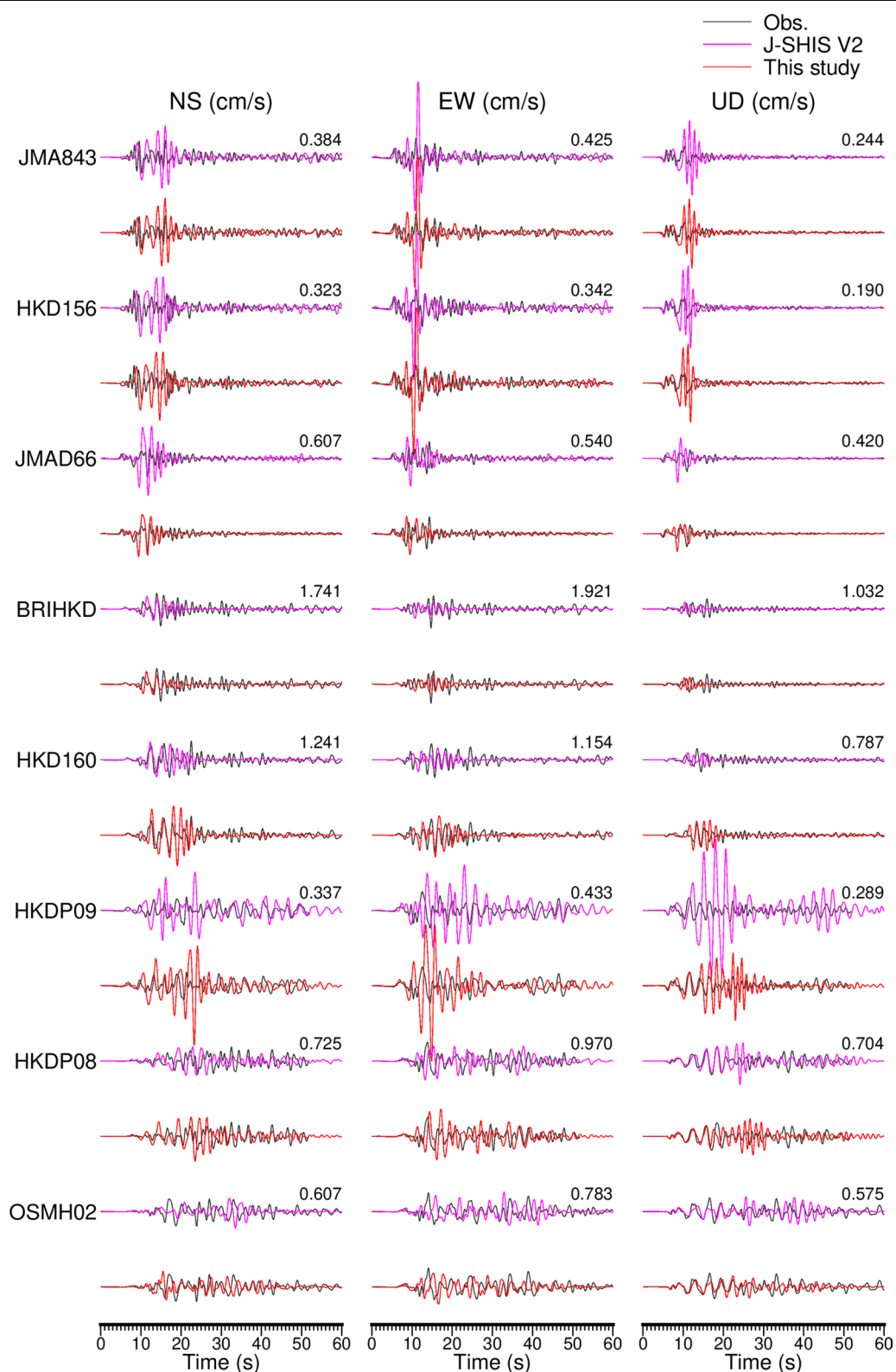


Fig. 11 Comparison of observed and simulated velocity waveforms. The observed velocity waveforms are plotted with gray lines. The simulated waveforms with J-SHIS V2 model and our new model are plotted with purple lines and red lines, respectively. The waveforms are bandpass filtered at 0.1–1 Hz. The number placed above each trace is the maximum amplitude of the observed waveform in cm/s. The origin of the horizontal axis corresponds to the origin time of the earthquake determined by JMA

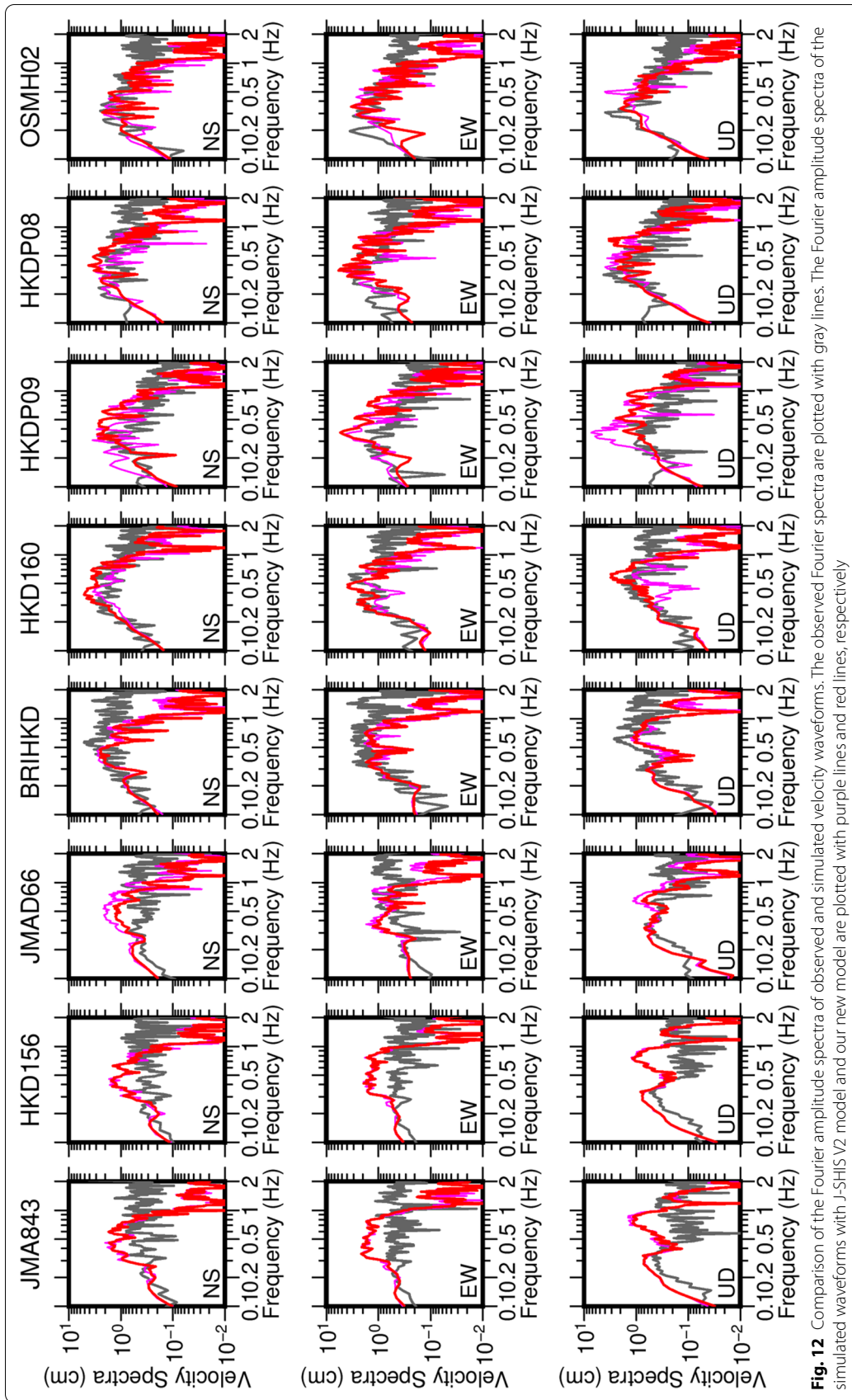


Fig. 12 Comparison of the Fourier amplitude spectra of observed and simulated velocity waveforms. The observed Fourier spectra are plotted with gray lines. The Fourier amplitude spectra of the simulated waveforms with J-SHS V2 model and our new model are plotted with purple lines and red lines, respectively

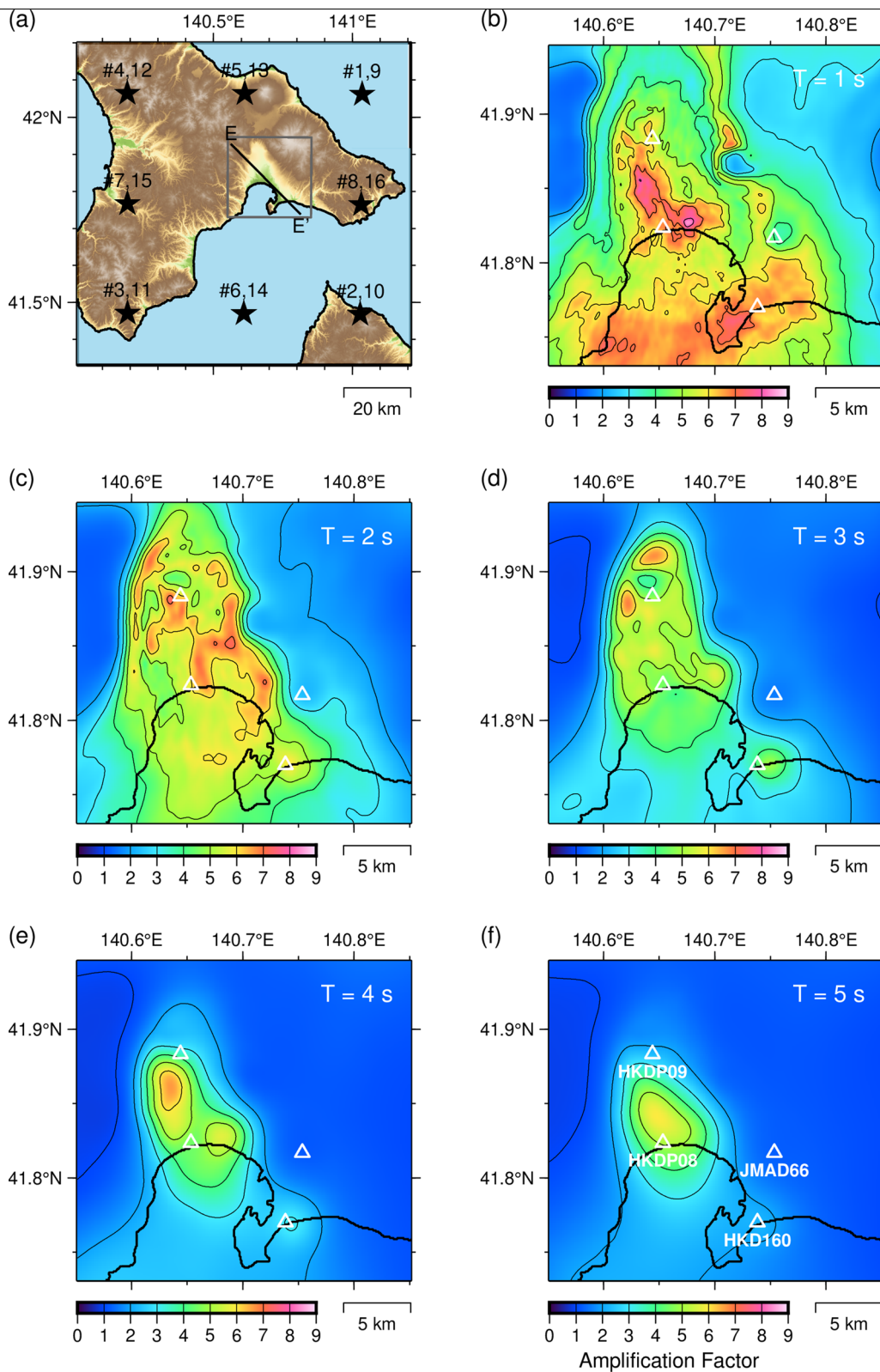


Fig. 13 (See legend on next page.)

(See figure on previous page.)

Fig. 13 The logarithmic mean of the amplification factor at each period. **a** The assumed source locations for numerical simulations of long-period ground motion amplification. The gray box represents the geographical area shown in **b–f**. The black solid line indicates the profile line E–E' along which the simulated waveforms are presented in Fig. 14. **b–f** The logarithmic mean of the amplification factor for the basin model relative to the rock model at each period. The open triangles indicate the sites shown in Fig. 15

Table 4 Locations of hypothetical sources for evaluating site amplification

Source no.	Latitude (°N)	Longitude (°E)	Depth (km)
#1	42.0618	141.0354	24.0
#2	41.4676	141.0282	24.0
#3	41.4702	140.1901	24.0
#4	42.0645	140.1896	24.0
#5	42.0639	140.6125	24.0
#6	41.4697	140.6092	24.0
#7	41.7673	140.1899	24.0
#8	41.7647	141.0317	24.0
#9	42.0618	141.0354	12.0
#10	41.4676	141.0282	12.0
#11	41.4702	140.1901	12.0
#12	42.0645	140.1896	12.0
#13	42.0639	140.6125	12.0
#14	41.4697	140.6092	12.0
#15	41.7673	140.1899	12.0
#16	41.7647	141.0317	12.0

was 2,306,352,600 (2,001 × 1,921 × 600). The time step in the FDM simulation was 0.0025 s. Further, we simulated a wavefield of 60 s from the origin time for each case. Figure 14 displays examples of simulated ground

velocity waveforms of the east–west component along a line across the Hakodate Plain for case #7. The simulated velocity waveforms of the basin model exhibited remarkable amplification inside the basin. Furthermore, the amplification was particularly large in the western part of the Hakodate Plain. The surface wave generated at the western edge of the basin can be observed between X=520 and 640 in this profile.

The amplitude spectrum of each component was obtained by the Fourier transform of the entire simulated waveform. The horizontal amplitude spectrum was obtained utilizing the root sum squares of the Fourier amplitude spectra of the two horizontal components. Furthermore, the amplification factor in the frequency domain is defined by the logarithmic mean of the spectral ratios:

$$\log[TF(f)] = \frac{1}{M} \sum_{i=1}^M \log \left[\frac{U_i(f)}{U_i^{\text{rock}}(f)} \right]. \tag{4}$$

$U_i(f)$ and $U_i^{\text{rock}}(f)$ are the horizontal amplitude spectra for the i th case by the simulation with the basin model and those with the rock model, respectively. Figure 13b–f exhibits the spatial distribution of the amplification factor $TF(f)$ at five different periods. As expected in the pasted-up waveforms in Fig. 14, the amplification is large

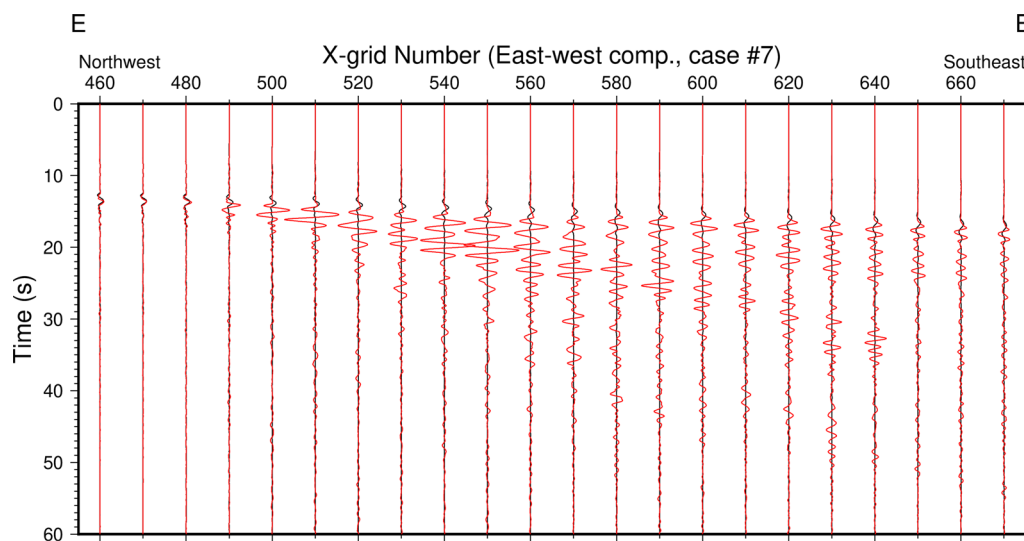


Fig. 14 Simulated velocity waveforms (0.1–2 Hz) along a profile line E–E' across the Hakodate Plain. The east–west components for case #7 (Table 4) are displayed. Red: basin model, black: rock model. The geographical location of the profile line E–E' is indicated in Fig. 13a

in the western part of the Hakodate Plain. The highest amplification at a period of 5 s was observed in the southwest area of the Hakodate Plain close to the coastline. In addition, a large amplification at a period of 4 s is distributed around that area. The amplification at a period of 3 s appears to be spatially uniform but slightly high near the western margin of the Hakodate Plain. The spatial characteristics of amplifications below 2 s were observed to be more complex than those of the longer period range.

Figure 15 displays the amplification factors for all cases and their logarithmic means at four representative sites in the plain. The standard deviation is large in a shorter period (higher frequency) due to the complexity of the seismic wavefield inside the basin owing to significant spatial variation in interference caused by differences in the source location. The logarithmic mean of the amplification factors for the entire waveform is larger than the theoretical one-dimensional amplification factor for the vertical incidence of SH-waves, particularly at higher frequencies. The peak frequency of the amplification factor based on the three-dimensional ground motion simulation differs from that of the one-dimensional amplification factor due to the three-dimensional basin effects except for JMAD66. Figure 16 also displays the logarithmic standard deviation of the amplification factor at each period, which further demonstrates a larger standard deviation in shorter periods (≤ 2 s).

The Holocene and late Pleistocene layers with S-wave velocities smaller than 0.6 km/s may also contribute to the amplification of ground motions in this period range in the Hakodate Plain. The existence of these low-velocity layers is obvious in our results pertaining to microtremor array surveys. However, we have not modeled the spatial distribution of these low-velocity layers in this study because the spatial information constraining them is presently not sufficient. Collection of boring logs and spatially dense microtremor observations of small arrays over the Hakodate Plain are required to overcome this limitation in subsequent research.

Conclusions

Small-to large-sized microtremor array surveys were carried out at five sites in the Hakodate Plain, southern Hokkaido, Japan, in order to estimate the S-wave velocity structure of sedimentary layers. The phase velocity was estimated at up to 5 Hz for the NNE site and 10 Hz for the remaining four sites. The observed phase velocity around 5 Hz was exceptionally low (approximately 65 m/s) at NNE, possibly due to the existence of loose peat or moor deposits. A site on the middle terrace (MHR) demonstrated a relatively larger phase

velocity at frequencies below 3 Hz. The one-dimensional S-wave velocity models were estimated by modeling the observed phase velocity dispersion curve with the fundamental mode of the Rayleigh wave. An additional layer of approximately $V_S=0.8$ km/s was required to reproduce the observed phase velocity at two sites in the western part of the Hakodate Plain. The estimated thickness of three layers of $V_S=0.6$, 1.1, and 1.4 km/s are relatively thick at two sites in the western part of the plain, consistent with the seismic reflection profiles (Sato et al. 2019) and the geological profiles at hot spring well (Geological Survey of Hokkaido 1995, 2004).

A new three-dimensional velocity model of the Hakodate Plain was developed by compiling the microtremor array surveys of this study and the reflection survey profiles of the Japan Oil Corporation (1981) and Sato et al. (2019). The velocity model consists of several homogeneous isotropic sedimentary layers ($V_S=0.6$, 1.1, 1.4, 1.7, and 2.1 km/s) above the basin bedrock ($V_S=2.7$ km/s), which expedites its incorporation into the nation-wide J-SHIS model. The bottom depth of the $V_S=0.6$ km/s layer corresponding to the bottom depth of Quaternary sediments is large along the western margin of the Hakodate Plain, reaching 0.56 km at the deepest location. The

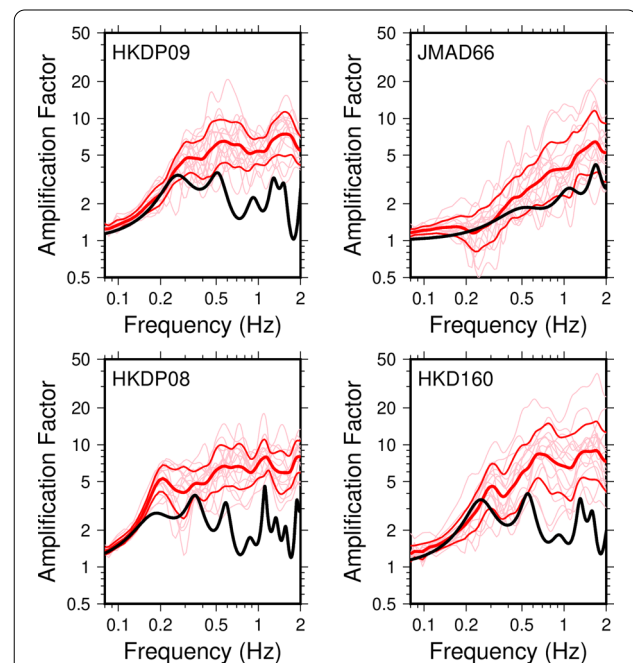


Fig. 15 Amplification factors at four sites in the Hakodate Plain. The site locations are specified in Fig. 13. Thin red lines represent the amplifications of the simulated waveforms from the basin model relative to the rock model for all numerical cases. The thick red line indicates their logarithmic mean and standard deviation. The black solid line corresponds to the theoretical amplification factor of the SH-wave with the vertical incidence

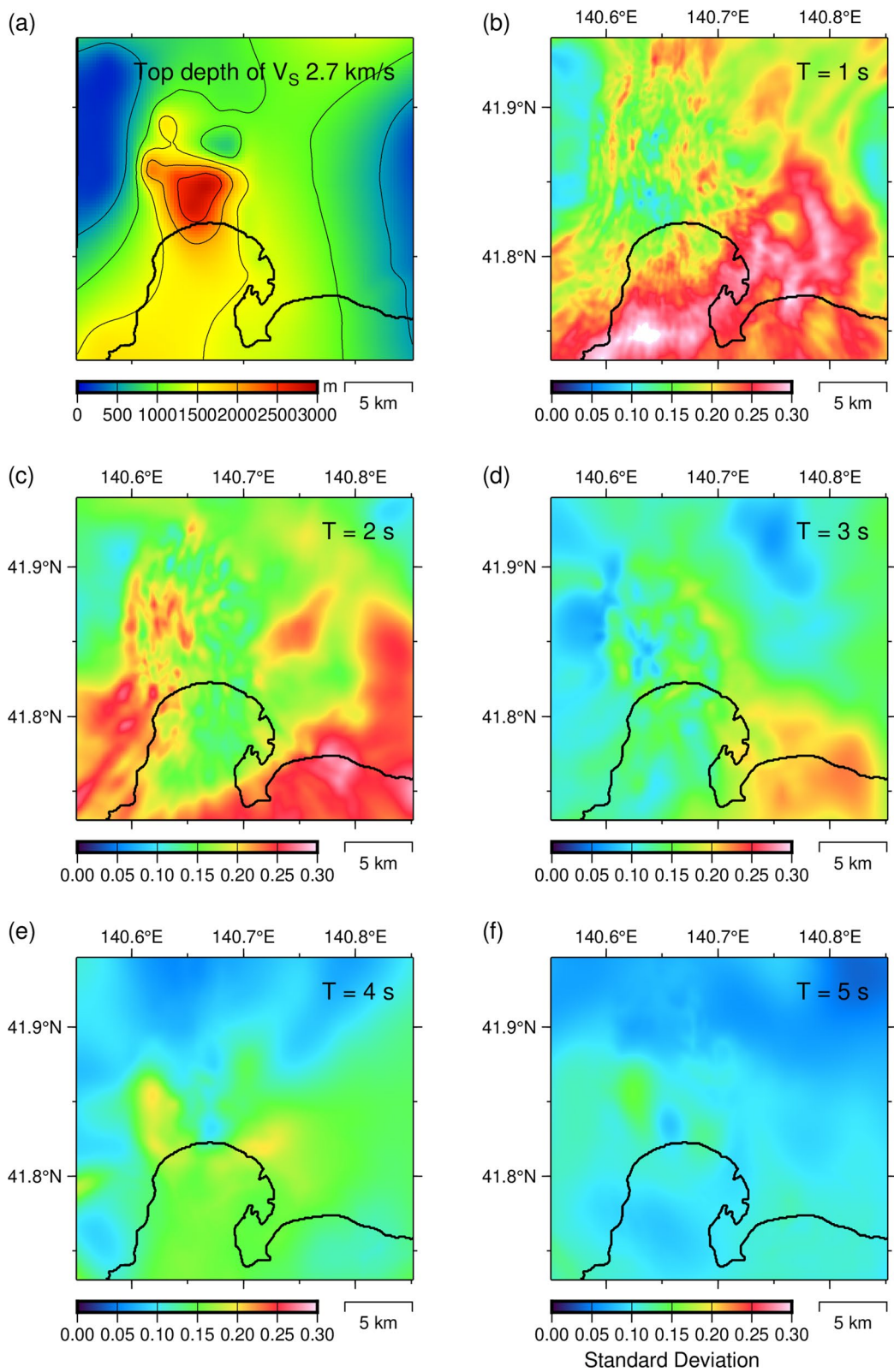


Fig. 16 The standard deviation of the amplification factor at each period. **a** The top depth of the layer for $V_s = 2.7 \text{ km/s}$ in and around the Hakodate Plain. **b–f** The standard deviation of the amplification factors at each period

bottom depths of $V_S = 1.1$ km/s and 1.4 km/s have similar tendencies. The bottom depth of $V_S = 1.7$ km/s layer deepens towards the coast in the western part of the Hakodate Plain, and its maximum depth is approximately 2.9 km. The total thickness of the sedimentary layers was relatively small on the eastern margin of the plain.

The newly developed three-dimensional velocity model has been validated via gravity anomaly modeling and numerical ground motion simulation of a moderate-sized inland earthquake (M_W 5.2). The gravity anomaly modeling showed improvement of the spatial distribution of the low-gravity anomaly around the coastline of the Hakodate Bay. The numerical ground motion simulation (< 2 Hz) also demonstrated that the simulated waveforms and amplitude spectra have been improved in terms of the amplitude and ground motion duration using the new model compared to the existing J-SHIS V2 model except stations located at the northern end of the Hakodate Plain, where no data has been available to constrain the three-dimensional velocity model. The evaluation of waveform fits, and spectral fits also suggested that modeling of near-surface low-velocity layers ($V_S < 0.6$ km/s) would be required for further improving the simulation results in higher frequency range (> 1 Hz).

Then, the spatial variation in long-period ground motion amplifications was discussed based on numerical ground motion simulation using this velocity model. The logarithmic mean of the amplification factors for the entire waveform is observed to be larger than the theoretical one-dimensional amplification factor for the vertical incidence of SH-waves, particularly at higher frequencies. The highest amplification at a period of 5 s was observed close to the coastline in the western part of the Hakodate Plain, where the bedrock depth was the deepest. The area of large amplification at a period of 4 s was distributed around that area. The amplification at a period of 3 s was relatively smooth in space and slightly high near the western margin of the plain. The spatial characteristics of amplifications below 2 s were quite complex due to interference of the seismic wavefield inside the basin structure. In addition, the logarithmic standard deviation among 16 synthetic cases was also observed to be large in the shorter period range. The quantitative modeling of near-surface low-velocity layers ($V_S < 0.6$ km/s) would also be necessary for further development of ground motion predictions in the Hakodate Plain.

Abbreviations

AIST: National Institute of Advanced Industrial Science and Technology; ERC: Earthquake Research Committee; FDM: Finite difference method; GA: Genetic algorithm; GOF: Goodness-of-fit; GSJ: Geological Survey of Japan; HERP: Headquarters for Earthquake Research Promotion; JMA: Japan Meteorological

Agency; J-SHIS: Japan Seismic Hazard Information Station; JST: Japan Standard Time; MEXT: Ministry of Education, Culture, Sports, Science, and Technology; NIED: National Research Institute for Earth Science and Disaster Resilience; PGV: Peak ground velocity; SPAC: Spatial autocorrelation; UTC: Coordinated Universal Time.

Supplementary Information

The online version contains supplementary material available at <https://doi.org/10.1186/s40623-022-01647-w>.

Additional file 1: Table S1. Search ranges of parameters in the GA search for each observation site. **Fig. S1.** Array configurations at HAK site in Hakodate city. Red, green, and blue symbols and lines correspond to L array, S array, and N array, respectively. The circles indicate the locations of sensors. The black inverted triangle represents K-NET HKD160 strong motion station. **Fig. S2.** Array configurations at MHR site in Mihara, Hakodate city. Red, green, and blue symbols and lines correspond to L array, S array, and N array, respectively. The circles indicate the locations of sensors. The black inverted triangle represents JMA D66 strong motion station. **Fig. S3.** Array configurations at KMI site in Kamiiso, Hokuto city. Red, green, and blue symbols and lines correspond to L array, S array, and N array, respectively. The circles indicate the locations of sensors. The black inverted triangle represents HKDP08 strong motion station. **Fig. S4.** Array configurations at OON site in Ono, Hokuto city. Red, green, and blue symbols and lines correspond to L array, S array, and N array, respectively. The circles indicate the locations of sensors. The black inverted triangle represents HKDP09 strong motion station. **Fig. S5.** Array configurations at NNE site in Nanae town. Red, green, and blue symbols and lines correspond to L array, S array, and N array, respectively. The circles indicate the locations of sensors. The black square represents the location of the hot-spring well (H480-017). **Fig. S6.** Photo of the huddle test on September 25, 2017, at Omori Park in Hakodate city. Eight blue cylindrical-shaped sensors are LE-3D/5s manufactured by Lennartz-Electronic (one was for spare, which was not used in this field work). Data loggers DATAMARK LS-8800 connected to LE-3D/5s are stored in orange boxes. Four duralumin boxes are portable all-in-one accelerographs SMAR-6A3P (three accelerometers and data logger LS-8800). **Fig. S7.** Results of the huddle test for LE-3D/5s sensors. (Top) Velocity waveforms of the vertical component observed by seven LE-3D/5s sensors (0.1–10 Hz). The origin time of the time axis is at 10:08:18.72 on September 25, 2017 (JST). (Bottom Left) Ensemble average of the power spectral densities of five selected time-windows of the vertical component for all seven sensors. (Bottom Right) Ensemble average of the coherences and phase differences of the vertical components for all possible combinations of the seven sensors. **Fig. S8.** Results of the huddle test for SMAR-6A3P seismographs. (Top) Acceleration waveforms of the vertical component observed by four SMAR-6A3P seismographs (0.1–10 Hz). The origin time of the time axis is at 10:04:56.16 on September 25, 2017 (JST). (Bottom Left) Ensemble average of the power spectral densities of five selected time-windows of the vertical component for all four sensors. (Bottom Right) Ensemble average of the coherences and phase differences of the vertical components for all possible combinations of the four sensors. **Fig. S9.** Comparison of the S-wave velocity model estimated by the microtremor array observation with the geological profile of nearby hot spring well (Geological Survey of Hokkaido 1995, 2004). The locations of the hot spring wells were shown in Fig. 1(a). H: Holocene, Fm: Fumizuki Formation, Tm: Tomikawa Formation, Tv: Togeshita pyroclastic rocks, Mh: Mohejigawa Formation, Td: Todagawa Formation, Hk: Hekirijigawa Formation, K: Kamiiso Group. **Fig. S10.** Goodness-of-Fit (GOF) scores evaluated for five frequency bands (0.05–0.1 Hz, 0.1–0.2 Hz, 0.2–0.5 Hz, 0.5–1 Hz, and 1–2 Hz) based on the GOF criterion proposed by Anderson (2004). The square, circle, and triangle correspond to NS, EW, and UD component, respectively. The number above each panel is the average of the GOF scores of all frequency bands and components. Red: This study, purple: J-SHIS V2 model.

Additional file 2. Observed phase velocity and its standard deviation at HAK in the CSV format.

Additional file 3. Observed phase velocity and its standard deviation at MHR in the CSV format.

Additional file 4. Observed phase velocity and its standard deviation at KMI in the CSV format.

Additional file 5. Observed phase velocity and its standard deviation at OON in the CSV format.

Additional file 6. Observed phase velocity and its standard deviation at NNE in the CSV format.

Additional file 7. The top depth of each velocity layer for each mesh in the three-dimensional velocity model in the Hakodate Plain constructed in this study in the CSV format.

Acknowledgements

The fieldwork in this study was assisted by Suqun Ling, Takashi Akazawa, Yujia Guo, Kenichi Konishi, Toshimitsu Nishimura, and Masahiro Takano. The authors appreciate Hiroshi Sato and Hidehiko Shimizu for providing us with their reflection and refraction tomography results. The authors greatly appreciate Masayoshi Ichiyanagi and Nobuo Takai for their help with the strong-motion waveform data of the Hokkaido Government. The Cray XC40 supercomputer (Camphor 2) of the Academic Center for Computing and Media Studies of Kyoto University was utilized in this study. Most figures were drawn using Generic Mapping Tools (Wessel et al. 2019). We appreciate the Lead Guest Editor, Masanao Shinohara, and two anonymous reviewers for their comments on our manuscript.

Author contributions

KA and TI designed the study. KA conducted the ground motion simulation and drafted the manuscript. TI collected seismic reflection survey results and strong motion data. KY organized the fieldwork and analyzed the microtremor array data. NI, KS, KY, and KM developed a three-dimensional velocity model, and the NI also performed gravity modeling. MO participated in the fieldwork and interpretation of the results. All authors read and approved the final manuscript.

Funding

Microtremor array surveys and construction of three-dimensional velocity structure modeling were conducted as a part of the Integrated Research Project on Seismic and Tsunami Hazards around the Sea of Japan funded by MEXT. A part of this work was also supported by the Second Earthquake and Volcano Hazards Observation and Research Program of MEXT and Grant-in-Aid for Scientific Research (C) 20K04084 from the Japan Society for the Promotion of Science.

Availability of data and materials

The microtremor observation records obtained in this study can be provided from the corresponding author upon reasonable request. The observed phase velocity data for each array site are provided as Additional files 2, 3, 4, 5, 6. The three-dimensional velocity model in the Hakodate Plain constructed in this study is provided as Additional file 7. The strong-motion waveform data pertaining to K-NET and KiK-net (Aoi et al. 2020; NIED 2019b) were provided by NIED via their website (<https://www.kyoshin.bosai.go.jp/>). The strong-motion waveform data in relation to JMA were released from the Japan Meteorological Business Support Center. The strong-motion waveform data from the seismic intensity observation network of the Hokkaido Government were provided with written permission from the Hokkaido Government. The strong-motion waveform data of the Building Research Institute are available at <https://smo.kenken.go.jp/>. The JMA unified hypocenter catalog was published as the Seismological Bulletin of Japan by JMA in collaboration with MEXT (https://www.data.jma.go.jp/svd/eqev/data/bulletin/index_e.html). The NIED F-net moment tensor catalog (NIED 2019a) is open to the public at <https://www.fnet.bosai.go.jp/top.php?LANG=en>. The Gravity Database of Japan (Geological Survey of Japan 2013) is available on the GSJ website (https://www.gsj.jp/Map/EN/cd_dvd_list.html). The J-SHIS V2 model (NIED 2019c) was downloaded from the NIED J-SHIS website at <https://www.j-shis.bosai.go.jp/en/>. The vector shape files of the Seamless Digital Geological Map of Japan 1: 200,000 V2 (Geological Survey of Japan 2020) was downloaded from their website (https://gbank.gsj.jp/seamless/index_en.html). The 10 m mesh digital elevation model in the Digital Map (Basic Geospatial Information) published by the Geospatial Information Authority of Japan was utilized to draw maps. The Japanese National Oil Corporation's reflection survey results were

disclosed by the Japan Oil, Gas and Metals National Corporation (JOGMEC) (http://www.jogmec.go.jp/oilgas/field_surveys_002.html).

Declarations

Ethics approval and consent to participate

Not applicable.

Consent for publication

Not applicable.

Competing interests

The authors declare that they have no competing interests.

Author details

¹Disaster Prevention Research Institute, Kyoto University, Gokasho, Uji, Kyoto 611-0011, Japan. ²Geo-Research Institute, Kokuminkaikan Osakajo Bldg. 6th floor, 2-1-2 Otemae, Chuo-ku, Osaka 540-0008, Japan. ³Research Institute of Nuclear Engineering, University of Fukui, 1-3-33 Kanawa-cho, Tsuruga, Fukui 914-0055, Japan.

Received: 15 October 2021 Accepted: 16 May 2022

Published online: 17 June 2022

References

- Aagaard BT, Brocher TM, Dolenc D, Dreger D, Graves RW, Harmsen S, Hartzell S, Larsen S, Zoback ML (2008) Ground-motion modeling of the 1906 San Francisco earthquake, part I: validation using the 1989 Loma Prieta earthquake. *Bull Seismol Soc Am* 98:989–1011. <https://doi.org/10.1785/0120060409>
- Aki K (1957) Space and time spectra of stationary stochastic waves, with special reference to microtremors. *Bull Earthq Res Inst Univ Tokyo* 35:415–457. <https://doi.org/10.15083/0000033938>
- Ali A, Kim KY (2018) Comparative analysis of seismic site conditions and microzonation of the major cities in Gangwon Province, Korea. *Explor Geophys* 49:176–186. <https://doi.org/10.1071/EG16136>
- Anderson JG (2004) Quantitative measure of the goodness-of-fit of synthetic seismograms. In: Proceedings of the 13th world conference on earthquake engineering, Vancouver, BC, Canada, 1–6 August 2004
- Aoi S, Asano Y, Kunugi T, Kimura T, Uehira K, Takahashi N, Ueda H, Shiomi K, Matsumoto T, Fujiwara H (2020) MOWLAS: NIED observation network for earthquake, tsunami and volcano. *Earth Planets Space* 72:126. <https://doi.org/10.1186/s40623-020-01250-x>
- Apostolidis P, Raptakis D, Roumelioti Z, Pitilakis K (2004) Determination of S-wave velocity structure using microtremor and SPAC method applied in Thessaloniki (Greece). *Soil Dyn Struct Eng* 24:49–67. <https://doi.org/10.1016/j.soildyn.2003.09.001>
- Arai H, Tokimatsu K (2008) Three-dimensional V_s profiling using microtremors in Kushiro, Japan. *Earthq Eng Struct Dyn* 37:845–859. <https://doi.org/10.1002/eqe.788>
- Asano K, Iwata T, Miyakoshi K, Ohori M (2015) Study on underground velocity structure model in the Kaga Plain and the Ochigata Plain using microtremor observations. *J Jpn Assoc Earthq Eng* 15(7):194–204. https://doi.org/10.5610/jaee.15.7_194 (in Japanese with English abstract)
- Asano K, Sekiguchi H, Iwata T, Yoshimi M, Hayashida T, Saomoto H, Horikawa H (2016) Modelling of wave propagation and attenuation in the Osaka sedimentary basin, western Japan, during the 2013 Awaji Island earthquake. *Geophys J Int* 204:1678–1694. <https://doi.org/10.1093/gji/ggv543>
- Chimoto K, Yamanaka H, Tsuno S, Miyake H, Yamada N (2016) Estimation of shallow S-wave velocity structure using microtremor array exploration at temporary strong motion observation stations for aftershocks of the 2016 Kumamoto earthquake. *Earth Planets Space* 68:206. <https://doi.org/10.1186/s40623-016-0581-3>
- Earthquake Research Committee (2021a) Revision of Probability of Earthquake Occurrence in Long-Term Evaluation. Headquarters for Earthquake Research Promotion, Tokyo. https://www.jishin.go.jp/evaluation/long_

- [term_evaluation/chousa_21jan_kakuritsu_index/](#). Accessed 16 June 2021
- Earthquake Research Committee (2021b) National Seismic Hazard Map for Japan 2020. Headquarters for Earthquake Research Promotion, Tokyo. https://www.jishin.go.jp/evaluation/seismic_hazard_map/shm_report/shm_report_2020. Accessed 16 June 2021
- Foti S, Parolai S, Albarello D, Picozzi M (2011) Application of surface-wave methods for seismic site characterization. *Surv Geophys* 32:777–825. <https://doi.org/10.1007/s10712-011-9134-2>
- Fujiwara H, Kawai S, Aoi S, Morikawa N, Senna S, Azuma H, Ooi M, Hao KX, Hasegawa N, Maeda T, Iwaki A, Wakamatsu K, Imoto M, Okumura T, Matsuyama H, Narita A (2012) Some Improvements of Seismic Hazard Assessment based on the 2011 Tohoku Earthquake. Technical note of the National Research Institute for Earth Science and Disaster Prevention 379. <https://doi.org/10.24732/nied.00001993> (in Japanese)
- Geological Survey of Hokkaido (1995) Geothermal development of local governments in Hokkaido: well data and thermal utilization 1980–1993. Geological Survey of Hokkaido, Sapporo (in Japanese)
- Geological Survey of Hokkaido (2004) List for the geothermal well drilling of governments in Hokkaido. Geological Survey of Hokkaido, Sapporo (in Japanese)
- Geological Survey of Japan (eds.) (2013) Gravity database of Japan, DVD edition. Digital Geoscience Map, P-2. Geological Survey of Japan, AIST, Tsukuba
- Geological Survey of Japan, AIST (2020) Seamless digital geological map of Japan 1: 200,000 V2, April 6, 2020 version. Geological Survey of Japan, AIST, Tsukuba. <https://gbank.gsj.jp/seamless/>. Accessed 6 Jan 2022
- Goto H, Takahashi C, Ishii Y, Ling S-Q, Miyakoshi K, Morikawa H, Sato Y, Sawada S, Shingaki Y, Suzuki Y, Takabatake D, Joshima M (2009) Deep subsurface structure estimated by microtremors array observations and gravity surveys in Kashiwazaki area, Japan. *Soils Found* 49:651–659. <https://doi.org/10.3208/sandf.49.651>
- Graves RW (1996) Simulating seismic wave propagation in 3D elastic media using staggered-grid finite differences. *Bull Seismol Soc Am* 86:1091–1106. <https://doi.org/10.1785/BSSA0860041091>
- Hata M, Uemura F, Hiroshima T (1984) Geological Map of Japan 1:200,000, Hakodate and Oshima-O-Shima. Geological Survey of Japan, Tsukuba. <https://gbank.gsj.jp/ld/resource/geolis/99905025>. Accessed 6 Jan 2022
- Hatayama K, Kanno T, Kudo K (2007) Control factors of spatial variation of long-period strong ground motions in the Yufutsu sedimentary basin, Hokkaido, during the M_w 8.0 2003 Tokachi-oki, Japan, earthquake. *Bull Seismol Soc Am* 97:1308–1323. <https://doi.org/10.1785/0120060200>
- Hayashi S, Katayama T (1970) Damage to harbour structures by the Tokachioki earthquake. *Soils Found* 10:83–102. https://doi.org/10.3208/sandf1960.10.2_83
- Ichiyanagi M, Takada M, Takahashi H (2017) Seismic activity associated with the 2016 Minamikayabe earthquake (M_{max} 5.3) in southern Hokkaido, Japan. *Geophys Bull Hokkaido Univ* 80:1–11. <https://doi.org/10.14943/gbhu.80.1>
- Japan Meteorological Agency (2020) The seismological bulletin of Japan. Japan Meteorological Agency, Tokyo. https://www.data.jma.go.jp/svd/eqev/data/bulletin/index_e.html. Accessed 13 July 2021
- Japan National Oil Corporation (1981) Report on basic geophysical exploration in Oshima Peninsula area in 1980. Japan National Oil Corporation, Tokyo (in Japanese)
- Kanamori H (1971) Focal mechanism of the Tokachi-oki earthquake of May 16, 1968: contortion of the lithosphere at a junction of two trenches. *Tectonophysics* 12:1–13. [https://doi.org/10.1016/0040-1951\(71\)90063-1](https://doi.org/10.1016/0040-1951(71)90063-1)
- Kikuchi M, Fukao Y (1985) Iterative deconvolution of complex body waves from great earthquakes—the Tokachi-oki earthquake of 1968. *Phys Earth Planet Int* 37:235–248. [https://doi.org/10.1016/0031-9201\(85\)90011-1](https://doi.org/10.1016/0031-9201(85)90011-1)
- Kudo K, Kanno T, Okada H, Ozel O, Erdik M, Sasatani T, Higashi S, Takahashi M, Yoshida K (2002) Site-specific issues for strong ground motions during the Kocaeli, Turkey, earthquake of 17 August 1999, as inferred from array observations of microtremors and aftershocks. *Bull Seismol Soc Am* 92:448–465. <https://doi.org/10.1785/0120000812>
- Ling S, Okada H (1993) An extended use of the spatial autocorrelation method for the estimation of geological structure using microtremors. In: Proceedings of the 89th SEGJ conference, Nagoya, Japan, 12–14 October 1993
- Ludwig WJ, Nafe JE, Drake CL (1970) Seismic refraction. In: Maxwell AE (ed) *The sea: ideas and observations on progress in the study of the seas*, vol 4 Part 1. Wiley, New York, pp 53–84
- Mascandola C, Massa M, Barani S, Albarello D, Lovati S, Martelli L, Poggi V (2019) Mapping the seismic bedrock of Po Plain (Italy) through ambient-vibration monitoring. *Bull Seismol Soc Am* 109:164–177. <https://doi.org/10.1785/0120180193>
- Miyakoshi K, Nishimura T, Yamada K, Tsuno S, Korenaga M, Ling S (2021) Subsurface velocity structural model in the northern part of the Osaka sedimentary basin by integrated interpretation of the microtremor array survey and seismic reflection survey. *BUTSURI-TANSA (Geophys Explor)* 74:17–29. <https://doi.org/10.3124/segj.74.17> (in Japanese with English abstract)
- Miyakoshi K, Okada H, Ling S (1996) A range of wavelengths possible to estimate phase velocities of surface waves in microtremors. In: Proceedings of the 94th SEGJ conference, Tokyo, Japan, 15–17 May 1996
- Mori J, Shimazaki K (1985) Inversion of intermediate-period Rayleigh waves for source characteristics of the 1968 Tokachi-Oki earthquake. *J Geophys Res* 90:11374–11382. <https://doi.org/10.1029/JB090iB13p11374>
- National Institute of Advanced Industrial Science and Technology (2019) Active Fault Database of Japan, April 26, 2019 version. Research Information Database, DB095. National Institute of Advanced Industrial Science and Technology, Tsukuba. <http://gbank.gsj.jp/activefault/>. Accessed 7 Oct 2020
- National Research Institute for Earth Science and Disaster Resilience (2019a) NIED F-net. National Research Institute for Earth Science and Disaster Resilience, Tsukuba. <https://doi.org/10.17598/nied.0005>
- National Research Institute for Earth Science and Disaster Resilience (2019b) NIED K-NET, KIK-net. National Research Institute for Earth Science and Disaster Resilience, Tsukuba. <https://doi.org/10.17598/nied.0004>
- National Research Institute for Earth Science and Disaster Resilience (2019c) J-SHIS Japan seismic hazard information station. National Research Institute for Earth Science and Disaster Resilience, Tsukuba. <https://doi.org/10.17598/nied.0010>
- Nogoshi M, Igarashi T (1971) On the amplitude characteristics of microtremor (part 2). *Zisin (J Seismol Soc Jpn 2nd Ser)* 24:26–40. https://doi.org/10.4294/zisin.1948.24.1_26 (in Japanese with English abstract)
- Ohuri M, Nobata A, Wakamatsu K (2002) A comparison of ESAC and FK methods of estimating phase velocity using arbitrarily shaped microtremor arrays. *Bull Seismol Soc Am* 92:2323–2332. <https://doi.org/10.1785/0119980109>
- Okada H (2003) The microtremor survey method. Geophysical monograph series, no 12. Society of Exploration Geophysicists, Tulsa. <https://doi.org/10.1190/1.9781560801740>
- Okada H, Matsushima T, Moriya T, Sasatani T (1990) An exploration technique using long-period microtremors for determination of deep geological structures under urbanized areas. *BUTSURI-TANSA (Geophys Explor)* 43:402–417 (in Japanese with English abstract)
- Ota Y, Sato M, Research Group for Active Fault on the Oshima Peninsula (1994) Geomorphic history of the Hakodate Plain south Hokkaido, Japan with special reference to active faulting. *Quat Res (Daiyonki-Kenkyu)* 33:243–259. <https://doi.org/10.4116/jaqua.33.243> (in Japanese with English abstract)
- Plouff D (1976) Gravity and magnetic fields of polygonal prisms and application to magnetic terrain corrections. *Geophysics* 41:727–741. <https://doi.org/10.1190/1.1440645>
- Rosa-Cintas S, Galiana-Merino JJ, Molina-Palacios S, Rosa-Herranz J, García-Fernández M, Jiménez ML (2011) Soil characterization in urban areas of the Bajo Segura Basin (Southeast Spain) using H/V, F-K, and ESAC methods. *J Appl Geophys* 75:543–557. <https://doi.org/10.1016/j.jappgeo.2011.07.019>
- Saito M (1988) DISPER80: a subroutine package for the calculation of seismic normal mode solutions. In: Doornbos DJ (ed) *Seismological algorithms: computational methods and computer programs*. Academic Press, London
- Sato H, Ishiyama T, Kato N, Shimizu H, Sato T, Kawasaki S, No T, Kodaira S, Miura S (2019) Deep seismic reflection profiling across the Oshima Peninsula, SW Hokkaido, Japan. In: Abstracts of Japan Geoscience Union Meeting 2019, Chiba, 26–30 May 2019
- Shibata T, Takahashi T, Okazaki N, Ohtsu S, Suzuki T, Akita F (2009) Flow system of thermal water in the Hakodate Plain, Hokkaido. *Rep Geol Surv Hokkaido* 80:27–37 (in Japanese with English abstract)

- Smith WHF, Wessel P (1990) Gridding with continuous curvature splines in tension. *Geophysics* 55:293–305. <https://doi.org/10.1190/1.1442837>
- Special Committee for the Investigation of the Tokachi-oki Earthquake 1968 (1969) Report on the Tokachi-oki Earthquake 1968, Hokkaido, Japan. Special Committee for the Investigation of the Tokachi-oki Earthquake 1968, Sapporo (in Japanese)
- Tajika J, Ohtsu S, Okazaki N, Suzuki T, Hirakawa K, Fusejima Y (1999) Hakodate-Heiwa-Seien Fault Zone. Map Series of Active Faults in Hokkaido, No. 2. Geological Survey of Hokkaido, Sapporo
- Takahashi K, Tsuji T, Ikeda T, Nimiya H, Nagata Y, Suemoto Y (2019) Underground structures associated with horizontal sliding at Uchinomaki hot springs, Kyushu, Japan, during the 2016 Kumamoto earthquake. *Earth Planets Space* 71:87. <https://doi.org/10.1186/s40623-019-1066-y>
- Takai N, Shigefuji M, Horita J, Nomoto S, Maeda T, Ichianagi M, Takahashi H, Yamanaka H, Chimoto K, Tsuno S, Korenaga M, Yamada N (2019) Cause of destructive strong ground motion within 1–2 s in Mukawa town during the 2018 M_w 6.6 Hokkaido eastern Iburī earthquake. *Earth Planets Space* 71:67. <https://doi.org/10.1186/s40623-019-1044-4>
- Takanami T, Yamauchi M (1996) Shallow crustal structure derived from explosion seismic observations by using quarry blasts in the southernmost part of the Oshima peninsula, Hokkaido, Japan. *Geophys Bull Hokkaido Univ* 59:189–209. <https://doi.org/10.14943/gbhu.59.189>
- Wessel P, Luis JF, Uieda L, Scharroo R, Wobbe F, Smith WHF, Tian D (2019) The generic mapping tools version 6. *Geochem Geophys Geosys* 20:5556–5564. <https://doi.org/10.1029/2019GC008515>
- Xu P, Ling S, Ran W, Liu Q, Liu J (2013) Estimating Cenozoic thickness in the Beijing Plain area using array microtremor data. *Seismol Res Lett* 84:1039–1047. <https://doi.org/10.1785/0220130090>
- Yamada M, Cho I, Kuo C-H, Lin C-M, Miyakoshi K, Guo Y, Hayashida T, Matsumoto Y, Mori J, Yen Y-T, Kuo K-C (2020) Shallow subsurface structure in the Hualien basin and relevance to the damage pattern and fault rupture during the 2018 Hualien earthquake. *Bull Seismol Soc Am* 110:2939–2952. <https://doi.org/10.1785/0120200063>
- Yamanaka H, Ishida H (1996) Application of genetic algorithms to an inversion of surface-wave dispersion data. *Bull Seismol Soc Am* 86:436–444. <https://doi.org/10.1785/BSSA0860020436>
- Yoshida K, Uebayashi H (2020) Love-wave phase-velocity estimation from array-based rotational motion microtremor. *Bull Seismol Soc Am* 111:121–128. <https://doi.org/10.1785/0120200139>
- Yoshimi Y, Akagi T (1968) Tokachioki earthquake of 1968. *Soils Found* 8:87–95. https://doi.org/10.3208/sandf1960.8.3_87

Publisher's Note

Springer Nature remains neutral with regard to jurisdictional claims in published maps and institutional affiliations.

Submit your manuscript to a SpringerOpen[®] journal and benefit from:

- Convenient online submission
- Rigorous peer review
- Open access: articles freely available online
- High visibility within the field
- Retaining the copyright to your article

Submit your next manuscript at ► [springeropen.com](https://www.springeropen.com)
